



# Open Access Articles

## *Microwave backscattering from surf zone waves*

The Faculty of Oregon State University has made this article openly available.  
Please share how this access benefits you. Your story matters.

<b>Citation</b>	Catalán, P. A., M. C. Haller, and W. J. Plant. (2014). Microwave backscattering from surf zone waves. <i>Journal of Geophysical Research: Oceans</i> , 119, 3098–3120. doi:10.1002/2014JC009880
<b>DOI</b>	10.1002/2014JC009880
<b>Publisher</b>	American Geophysical Union
<b>Version</b>	Version of Record
<b>Terms of Use</b>	<a href="http://cdss.library.oregonstate.edu/sa-termsofuse">http://cdss.library.oregonstate.edu/sa-termsofuse</a>

## RESEARCH ARTICLE

## Microwave backscattering from surf zone waves

10.1002/2014JC009880

## Key Points:

- Breaking waves scatter energetically, regardless of polarization, wave, or wind
- NRCS of active breaking correlates well with Lambertian scattering
- Only one breaking event suffices to broaden Doppler spectra

## Correspondence to:

P. A. Catalán,  
patricio.catalan@usm.cl

## Citation:

Catalán, P. A., M. C. Haller, and W. J. Plant (2014), Microwave backscattering from surf zone waves, *J. Geophys. Res. Oceans*, 119, 3098–3120, doi:10.1002/2014JC009880.

Received 3 FEB 2014

Accepted 5 MAY 2014

Accepted article online 10 MAY 2014

Published online 28 MAY 2014

Patricio A. Catalán<sup>1,2,3</sup>, Merrick C. Haller<sup>4</sup>, and William J. Plant<sup>5</sup>
<sup>1</sup>Departamento de Obras Civiles, Universidad Técnica Federico Santa María, Valparaíso, Chile, <sup>2</sup>Centro Nacional de Investigación para la Gestión Integrada de Desastres Naturales, CONICYT/FONDAP/1511007, Santiago, Chile, <sup>3</sup>CCTVal-Centro Científico Tecnológico de Valparaíso, Basal Project FB021, Valparaíso, Chile, <sup>4</sup>Coastal & Ocean Engineering Program, School of Civil and Construction Engineering, Oregon State University, Corvallis, Oregon, USA, <sup>5</sup>Applied Physics Lab, University of Washington, Seattle, Washington, USA

**Abstract** The microwave backscatter properties of surf zone waves are analyzed using field observations. By utilizing a preexisting, independent, water surface discrimination technique, the microwave returns were extracted along individual waveforms and the data from shoaling (steepening) waves, surf zone breaking waves, and remnant foam were separated and quantified. In addition, a wave tracking analysis technique allows the returns to be examined on a wave-by-wave basis as individual waves progress through the shoaling zone and break on a nearshore sand bar. Normalized radar cross sections (NRCS), polarization ratios, Doppler spectra, and scatterer velocities were collected using a dual-polarized, X-band radar operating at lower grazing angles than previously reported ( $1^{\circ}$ – $3.5^{\circ}$ ). The results indicate that the maximum NRCS levels are from the active breaking portions of the wave and were consistently about  $-20$  dB, regardless of radar polarization, azimuth angle, wave height, or wind speed. In addition, breaking waves induce broadening of the Doppler spectra and mean scatterer velocities that correlate well with the carrier wave celerity. Analysis of the polarization ratios suggest that the active breaking portions of the wave are depolarized but that higher polarization ratios ( $>0$  dB) are found on the leading edges shoreward of the active breaking portions of the waves, which indicates a clear distinction between two scattering regimes. These results are consistent with scattering from a very rough surface that is being mechanically generated by the breaking process, showing a good agreement with the expected grazing angle dependency of a Lambertian scatterer.

## 1. Introduction

The nearshore portions of the ocean are unique areas where the presence of land (and shallow water) is a dominant influence on the hydrodynamic processes at play. Over the past few decades, there have been considerable efforts to utilize remote sensors to effectively sample this region [see Holman and Haller, 2013, for a review]. Parameters that are retrievable in a routine operational sense via radar remote sensing, include: bathymetry [e.g., Bell, 1999; Flampouris et al., 2008], wave directional distributions [e.g., Young et al., 1985; Frasier et al., 1995; Nieto Borge et al., 1999; Izquierdo and Guedes Soares, 2005], wave runup [Hasan and Takewaka, 2009], and surf zone morphology [e.g., Ruessink et al., 2002; McNinch, 2007]. In general, the retrieval of these parameters does not depend significantly on the details of the radar backscattering processes; hence, these were the first parameters to be operationalized.

However, more recently, efforts have been made to assimilate nearshore radar remote sensing data into numerical models [van Dongeren et al., 2008] and also use it for the estimation of alongshore currents [Perkovic et al., 2009], swash zone velocities [Puleo et al., 2003], water surface elevations [Dankert and Rosenthal, 2004], wave breaking [Farquharson et al., 2005; Catalán et al., 2011], surface wave fields [Nwogu and Lyzenga, 2010], and to monitor rip currents [Haller et al., 2014]. These applications are more dependent on the backscattering processes, especially those related to wave breaking. In surf zones, it is generally understood that wave breaking is the main process governing wave height variability and, more importantly, is the dominant hydrodynamic forcing mechanism. Hence, in order to identify wave breaking in radar returns and better utilize the measurements for the estimation of nearshore wave and current conditions, it is necessary to have a solid understanding of the radar backscatter processes from breaking versus nonbreaking waves in the nearshore.

Based on work primarily performed in intermediate and deep water wave regimes, and neglecting the contribution from wave breaking, microwave scattering from the ocean surface over a broad range of incidence

angles is well modeled by Composite Surface Theory (CST), whereby Bragg scattering is modulated by the two-scale ocean surface [Wright, 1968; Bass *et al.*, 1968]. The applicable range of incidence angles is from about 20° to 60° for vertical transmit and receive (VV polarization) but only from 20° to 45° for horizontal transmit and receive (HH polarization) [Plant *et al.*, 2010]. However, for deployments in the nearshore region, the viewing geometry is usually at large incidence angles (low grazing angles, LGA) and wave breaking occurs much more frequently; hence, previous research has shown that in this regime the scattering differs from CST predictions.

These differences from CST, i.e., scattering anomalies, are manifested as larger normalized radar cross sections (NRCS,  $\sigma_0$  in dB) than can be explained by CST. These large scattering events can also have relatively long durations and have traditionally been called sea spikes [e.g., Trizna, 1997]. Other aspects of spike events that deviate from CST include a broadening of the Doppler spectrum and a large offset of the expected Doppler velocities [e.g., Smith *et al.*, 1996; Lee *et al.*, 1995; Plant, 1997]. In addition, higher NRCS for HH polarization than for VV [e.g., Lewis and Olin, 1980; Frasier *et al.*, 1998] leads to polarization ratios,  $R_{HV} = \sigma_{0HH}/\sigma_{0VV}$ , exceeding unity [Trizna, 1991; Hwang *et al.*, 2008], which contradicts the CST prediction that  $R_{HV} < 1$ .

The source of these scattering anomalies are the least understood aspect of radar remote sensing, but the observational evidence clearly supports their association with breaking waves and/or steep (potentially incipient breaking) waves. A wide range of scattering models exists that can partially explain the observations, including wedge diffraction [Kalmykov and Pustovoytenko, 1976; Lyzenga *et al.*, 1983], the presence of plumes [Wetzel, 1986], or bound waves [Plant, 1997, 2003], specular reflection [Liu *et al.*, 1998], and multipath scattering [Sletten *et al.*, 1996; Trizna, 1997; West *et al.*, 1998; Plant *et al.*, 2010]. While all of these phenomena are reasonably thought to be associated with breaking waves, they are not fundamental characteristics of all breaking waves. Nor do they explicitly require the presence of rough, turbulent white water, and active dissipation, which is the nominal definition of wave breaking. On the other hand, the hydrodynamic forcing due to active breaking is considerably greater than that due to nonbreaking steep waves, especially in the nearshore [e.g., Svendsen, 2006]. Hence, the specific identification of active breaking is important.

Since a large portion of previous observations of scattering anomalies were collected in intermediate or deep water, assuming these results also apply to the surf zone would require that the hydrodynamics of wave breaking, the scattering mechanisms, and their relative contribution to the radar returns be the same in the two regions. However, there are several important differences between wave breaking in the nearshore versus offshore areas. For example, in the surf zone wave breaking is depth limited and persistent, and the size of the breaking crests is typically much larger than found in the offshore whitecapping regime. In addition, waves in the surf zone are mostly decoupled from the wind field and, finally, the relationship between the breaking wavelengths and their frequency is changed from that in deep water.

Despite these differences, only a handful of previous research has attempted to characterize the microwave scattering from surf zone waves. Among the earliest observations are those of Kalmykov *et al.* [1976] who attempted to relate the observed backscatter to the production of droplets by breaking waves. Lewis and Olin [1980] using a dual-polarized X-band sensor at 5° grazing found that sea spikes were well correlated with white water formation observed on synchronous optical data. A power differentiation between breaking and nonbreaking events was also observed, with the latter scattering about 15 dB less than the peak 1.7 dB at 9.2 GHz. Peak power of the spikes showed little polarization sensitivity and they suggested an isotropic mechanism from a very rough surface, such that the normalized scattering cross section would be directly related to the ratio of breaker area to the illuminated area. Subsequently, Phillips [1988] also proposed a model that assumed that NRCS was constant across whitecap areas. Haller and Lyzenga [2003] collected X-band (VV) observations of the surf zone, although at midincidence angles (31° and 46° grazing), and demonstrated that the backscattered power correlated well with the video-derived, areal coverage of the wave roller (the turbulent mass of air and water that propagates with broken waves in shallow water), which again supports a spatially constant normalized scattering cross section in the region of active breaking. In particular, their data suggested a spatially constant NRCS of  $-1.9$  dB at 31° grazing.

Puleo *et al.* [2003] collected surf (and swash) zone observations with a high-resolution (3 m range, 0.5° azimuth) Doppler radar. Although they focused on how the measured surface velocity signals compared with shallow water wave theory, they also observed that incipient breaking (very steep) waves could yield scattering levels similar to those of active breaking waves. In a subsequent study using the same data set,

Farquharson *et al.* [2005] found that peak NRCS of the observed breakers were typically in excess of  $-5$  dB at  $5^\circ$  grazing. These data were unique in that the observed NRCS exhibited a cross-shore decay as waves progressed shoreward through the surf, which corresponds to an increasing grazing angle. Although not developed explicitly for nearshore breaking waves, existing scattering models predict an increase in NRCS with grazing angle, for instance, wedge models [Lyzenga *et al.*, 1983], plumes [Wetzel, 1990], or bound waves [Plant, 1997]. However, Farquharson *et al.* [2005] associated this cross-shore decrease in the NRCS with the decay of a bore, modeled as a smooth scattering half-cylinder following Wetzel [1986]. Likely because they used a high-resolution system, they did not specifically analyze whether beam filling played a role as the size of the surf zone bores decayed across the surf zone. However, the wave conditions during their experiment were mild and the wavelengths were fairly short (water depth at breaking  $\sim 1$  m, peak period  $\sim 5.2$  s).

One aspect in the analysis of microwave scattering from breaking waves under field conditions that has always been a challenge, is identifying and separating the returns from the breaking versus nonbreaking portions of the water surface. Hand-in-hand with this issue is the relationship between the spatial scale of individual breakers and the spatial resolution of a given radar (i.e., beam filling) of which there is a wide variety. In the present work, we use an objective detection methodology that is based on the fusion of data from two remote sensors operating at very different frequencies (X-band and optical, see Catalán *et al.* [2011]). The identification method determines the time and space separation of the different stages of wave transformation (shoaling, breaking, remnant foam), which are then applied as a categorical filter in the analysis of radar backscatter from a synchronized research radar. The approach is similar to that of Liu *et al.* [1998] in deep water, who manually correlated and categorized radar spikes with surface features as observed within the entire field of view for a large number selected optical images. Here we improve this categorization by automating the process and by performing pixel-by-pixel categorizations. This also allows using the identification method to assess the influence of beam filling on the results.

We define three stages of the surf zone breaking cycle as the sources of interest. First, the shoaling stage, when intermediate/shallow water waves gradually grow higher and whose front face becomes gradually steeper. Next, active breaking, defined as the location of the wave roller where most of the organized wave energy dissipation takes place (hence relevant for nearshore hydrodynamics); and remnant foam corresponding to patches of turbulence, foam, and bubbles that are left behind the wave crest and can last for several wave periods. This methodology allows us to follow, on a wave-by-wave basis, the tempospatial evolution of a suite of standard microwave parameters. We focus our analysis on depth-limited breaking of gravity waves over an offshore sandbar, which allows us to analyze large-scale events at grazing angles in the range  $1^\circ$ – $3.5^\circ$ , thus lower grazing angles than those previously reported.

## 2. Experimental Data and Preliminary Processing

Nearshore remote sensing observations were collected over a 6 week period between 10 April and 22 May 2008 at the US Army Corp of Engineers Field Research Facility (FRF), Duck, NC during the Multi Remote Sensor Experiment in the NearShore Ocean (MR-SENSO). In the following, we utilize the FRF coordinate system (see Figure 1) where the cross-shore coordinate is denoted  $x$  and points offshore, the  $y$  coordinate points roughly  $18^\circ$  west of the north, and  $z = 0$  corresponds to NADV29. During the experiment, the beach profile had a relatively uniform alongshore bar at  $x = 300 - 400$  m, and the shoreline was located about  $x = 90 - 100$  m [Catalán *et al.*, 2011]. Data were collected using three remote sensors, focusing on the wave evolution as waves progressed over the offshore bar-trough system toward the shore. The first sensor, RiverRad, is an X-band (9.36 GHz), dual polarization (HH, VV) coherent radar developed by the Applied Physics Lab at the University of Washington [Plant *et al.*, 2005]. It was deployed on the crest of the dune at the north end of the FRF property, at  $x = 54.4$  m,  $y = 936.2$  m, and  $z = 10.2$  m. To maximize the overlapping area coverage with the other two sensors, the RiverRad acquisition scheme was set to collect observations along roughly 960 m range lines with a resolution of 7.5 m. Data were collected in a staring mode for 2 min, after which the antennas were mechanically rotated. A total of nine azimuthal locations separated by roughly  $10^\circ$  were used, resulting in the partial coverage of a circular sector of about  $80^\circ$ , spanning from a direct offshore look direction to a nearly alongshore look direction at the shoreline as shown in Figure 1. Clockwise and counterclockwise rotations were alternated and the system collected data almost continuously throughout the experiment. Data were delivered as received power and converted to NRCS  $\sigma_0(\theta, r, t)$ , by calibrating it against a standard reflector before and after the experiment. The Doppler spectrum and the

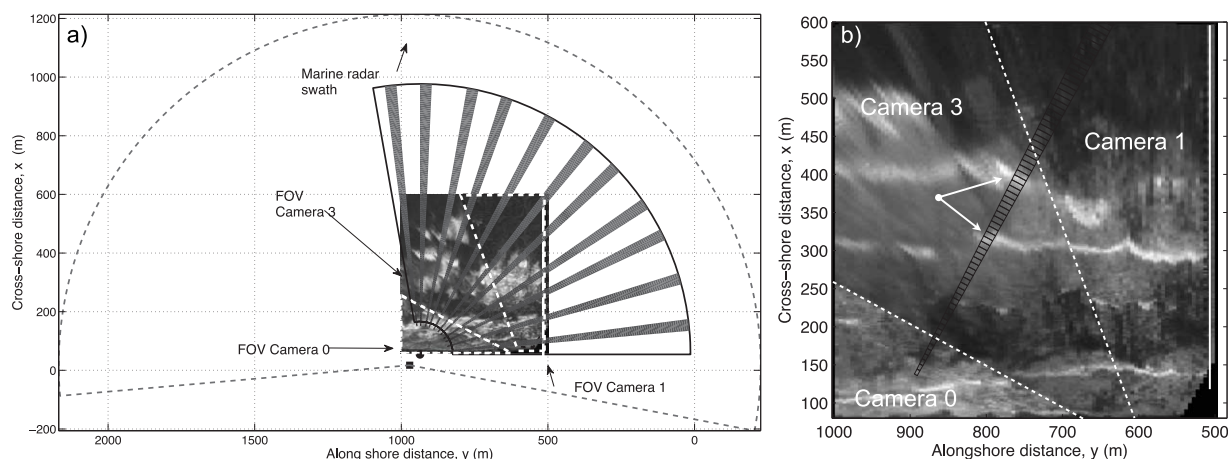


**Figure 1.** (a) Schematic of the field of view of the sensors and sensor location. Gray line arcs denote the swath covered by RiverRad (solid) and the marine radar (dashed), respectively. Background is merged images from the ARGUS III station where white dashed lines denote camera boundaries. The vertical white line indicates the location of the FRF pier, and the solid square and circle the location of the marine radar and RiverRad, respectively. Gray-shaded areas indicate the RiverRad swaths. (b) Zoom in of the video image. Black lines correspond to the RiverRad radar cells. White arrows indicate sample radar cells uniformly covered by active breaking.

Doppler offset at the spectral peak were recorded at each of the 128 range bins. A single Doppler spectrum averaged over the whole 2 min data collection was stored at each range bin, as well as 84 values of NRCS and Doppler offset at a sampling resolution of 0.53 s. The gain pattern characteristics of the antenna meant that upon calibration, NRCS values at ranges shorter than  $r = 200$  m where artificially increased and will not be considered in the analysis.

The second remote sensing system was comprised of three optical cameras from the ARGUS III observing station established at the FRF by the Coastal Imaging Lab, Oregon State University [see *Holman and Stanley, 2007*, for a review]. For the purpose of this experiment, a high-resolution rectangular pixel array was designed spanning  $x = 60$ – $600$  m and  $y = 500$ – $1000$  m with spatial resolution of  $\Delta x = 2$  m and  $\Delta y = 5$  m, using cameras 0, 3, and 1 as shown in Figure 1. Optical (video) pixel intensity data  $I(x, y, t)$  were collected at a sampling rate of 2 Hz for 31 min, hourly during daylight hours (seven collections per day).

Finally, the third sensor was a single polarization (HH polarized) marine radar operating at X-band (9.45 GHz). Data were collected hourly at a nominal rotation rate of 44 rpm or roughly 0.7 Hz, but only collections synchronous with the optical sets are used here. The large swath and synchronization of the optical and marine radar sensors allows the data to be used in conjunction to discriminate between the different stages of the breaking cycle on a wave-by-wave basis following the joint discrimination of *Catalán et al. [2011]*. The discrimination method is based on a heuristic model that can be summarized as follows: (1) active breaking is expected to be bright in both sensors, (2) remnant foam is optically bright but dark in the radar signal, and (3) very steep front faces of nonbreaking waves are bright in radar but dark in the optical signal. Since very steep fronts can yield very large backscattering levels [e.g., *Liu et al., 1998; Frasier et al., 1998; Puleo et al., 2003*], it is relevant to study how it compares against the scattering from breaking waves. Hence, an additional rule was added to the discrimination algorithm to discern very steep waves from the remaining nonbreaking waves. Since the optical signal of nonbreaking waves becomes darker as the wave becomes steeper [*Jähne et al., 1994*], this discrimination is achieved by defining a darkness threshold  $I_d^t$  for the optical data. The updated discrimination rule becomes [see *Catalán et al., 2011*, equation (3d)]:

$$I(x, y, t) < I_d^t \quad \& \quad \sigma_0(x, y, t) \geq \sigma_0^t, \quad (1)$$

where  $I_d^t$  is the optical intensity threshold to separate very steep waves and  $\sigma_0^t$  is the power threshold (in dB) for the marine radar record. From now on, we shall refer to these very steep waves simply as steep waves. The method is generally not sensitive to the values of the brightness thresholds used, and test discriminations by substituting the marine radar by RiverRad HH data instead yield similar results, ensuring the robustness of the scheme.



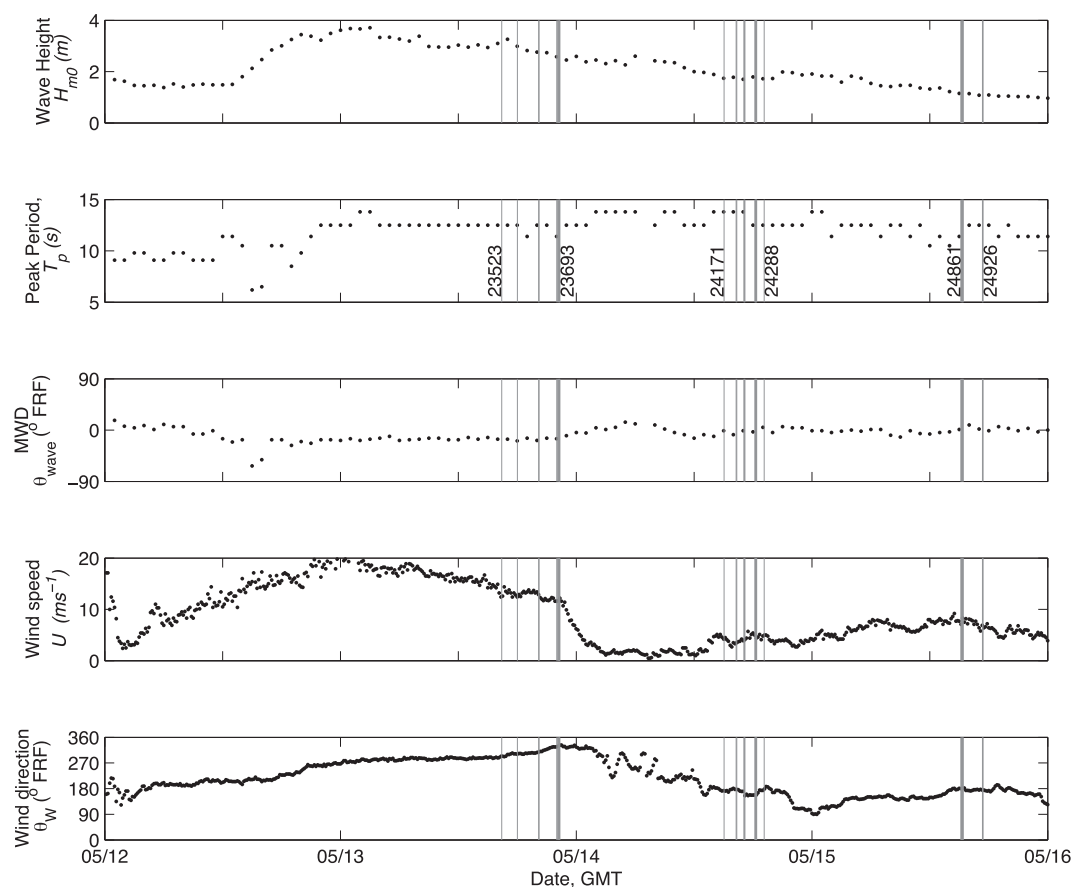


**Figure 2.** Wave and environmental conditions during data collection. Vertical gray lines indicate the RiverRad runs used in the analysis. (a) Significant wave height,  $H_{m0}$ ; (b) peak wave period,  $T_p$ ; (c) mean wave direction relative to the FRF x axis; (d) wind speed,  $U$ ; and (e) wind direction relative to the FRF x axis.

In the following, we focus the analysis on 31 RiverRad collection periods, which correspond to 11 sets of optical and marine radar data. In the following, each collection is identified based upon the sequential number of the RiverRad collection. The timing of the 31 RiverRad collections is indicated by light gray vertical lines in Figure 2, where sample collection identifiers are shown for reference.

These collections correspond to the decaying phase of a storm, when the environmental conditions showed large variability in significant wave height, wind speed, and wave direction, but wave period and wave direction remained fairly constant, as can be seen in Figure 2. Spatial coverage of remnant foam decayed as wave energy and wind speed decayed. We focus on azimuthal look directions spanning from  $\phi = -7^\circ$  to  $48^\circ$ , clockwise relative to the cross-shore axis.

The wave stage tag (breaking, steep, foam) for each instance was thus retrieved by table look up procedures and applied as a categorical filter on the RiverRad data, which allows us to examine the backscattering levels and other quantities as a function of scattering source. The time series of video and RiverRad HH were reduced and interpolated to the time and spatial domain of the RiverRad VV data, thus ensuring spatial and temporal pixel-to-pixel comparisons.

### 3. Results

We focus our attention on a set of standard microwave parameters and examine their dependence on the wave stage. These are the backscattered power at both polarizations (NRCS  $\sigma_{0HH}$  and  $\sigma_{0VV}$ , in dB), the polarization ratio ( $R_{HV} = \sigma_{0HH} / \sigma_{0VV}$ , in dB), the Doppler spectrum ( $S(f)$ , in dB), and Doppler offset (frequency of the Doppler spectral peak,  $f_D$ , in Hz) at each polarization. Given that RiverRad data are collected along fixed radial lines, time-space images (Hovmöller diagrams) along specific radials are used unless otherwise noted.

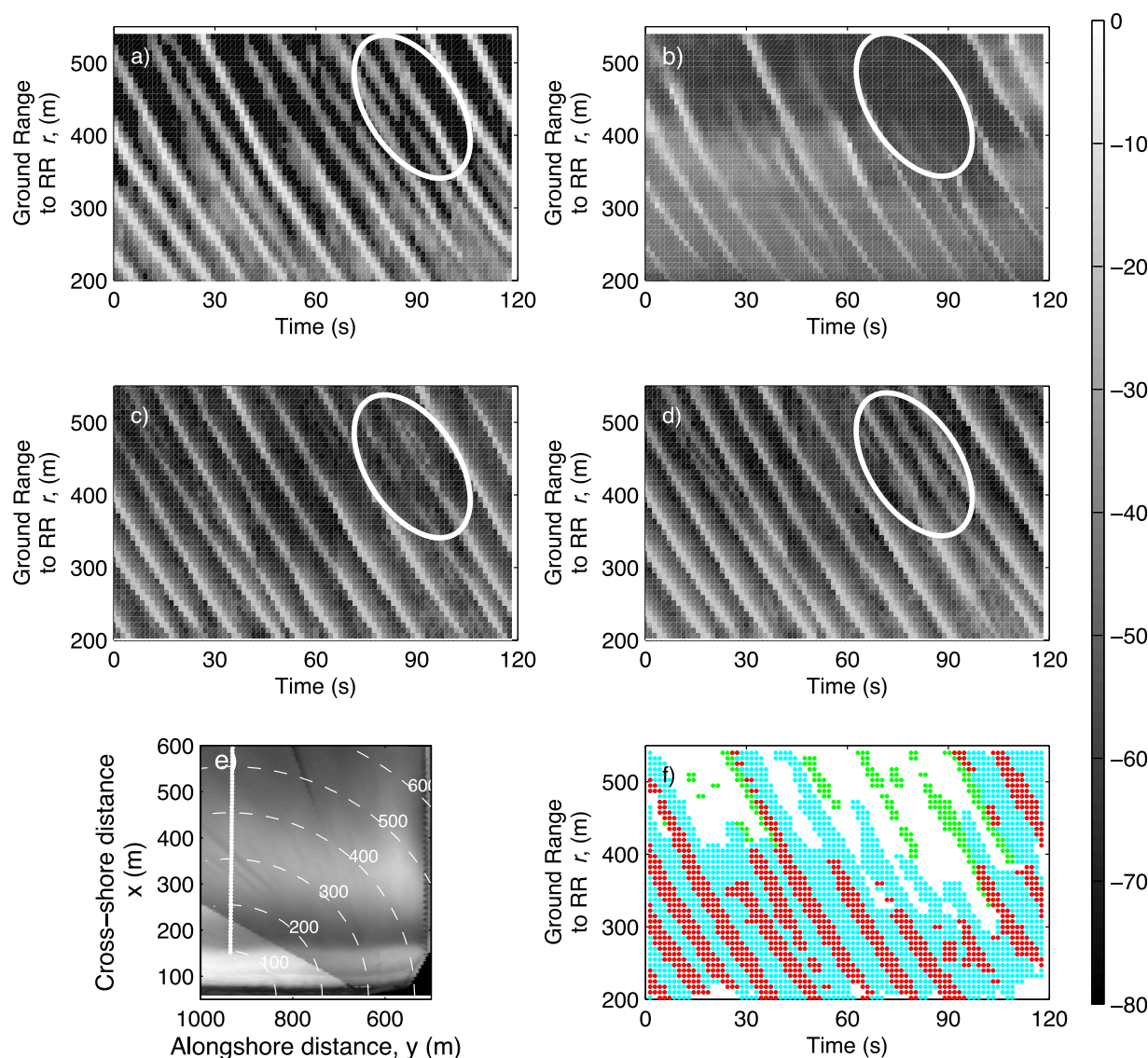


**Figure 3.** Sample time-space maps for collection 23688. (a) Marine radar calibrated,  $\sigma_0$  (dB); (b) optical pixel intensity,  $I$ ; (c) RiverRad,  $\sigma_{0HH}$  (dB); (d) RiverRad,  $\sigma_{0VV}$  (dB); (e) video time exposure showing the RiverRad look direction as dotted line. Arcs correspond to radial distances to RiverRad, (f) results of the breaking detection showing breaking (red\*), steep waves (green), and remnant foam (cyan) areas. Gray scale corresponds to the microwave NRCS (dB) for plots (a–d).

Time is given in seconds relative to the beginning of the RiverRad collection. The spatial coordinate  $r$ , in m, corresponds to the horizontal distance between the radar cell and RiverRad along the look direction (i.e., ground range).

Figure 3 shows sample time-space images of the calibrated marine radar  $\sigma_0$ , the optical intensity signal, and RiverRad  $\sigma_{0HH}$  and  $\sigma_{0VV}$ , along with the categorical filter results for collection 23688. The data indicate that almost all of the individual waves are breaking between  $r = 200 - 400$  m and, overall, the three radar images are very similar. However, shoaling waves offshore of breaking show somewhat larger  $\sigma_{0VV}$  signals than  $\sigma_{0HH}$  (compare Figure 3c and Figure 3d, as indicated by white ellipses at  $t = 75$  s and  $r = 500$  m), which would be expected within CST [e.g., Plant, 1990].

### 3.1. Breaking Detection

Figure 4 shows sample results of the detection algorithm for three different collections. Colored contours demarcating wave breaking, remnant foam, and steep waves are overlaid on the optical image. It can be

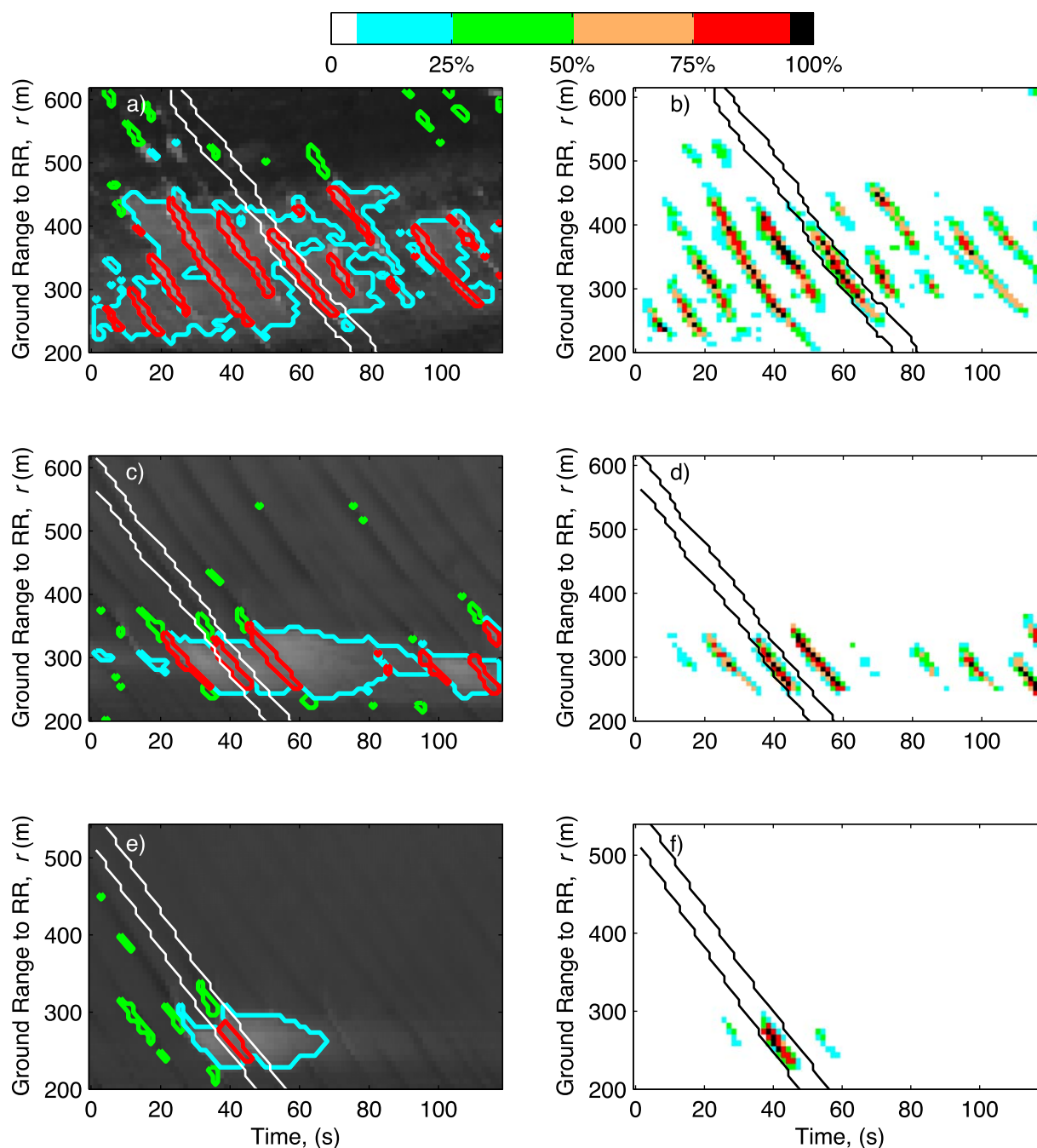


**Figure 4.** (left) Results of the breaking detection algorithm superimposed on their corresponding optical intensity images. Contours demarcate areas where  $BF_{\lambda}^* \geq 75\%$  for active breaking (red), steep events (green), and remnant foam (cyan). White contour indicates the trajectory of an individual wave, analyzed in section 3.2.1. (right) Beam filling fraction of the breaking waves expressed in percentage. Colorscale refers to right plots. (a–b) Collection 23691, (c–d) Collection 24863, and (e–f) Collection 24868.

seen that a visually pleasing discrimination is achieved throughout most of the field of view, especially between active breaking and remnant foam.

Previous studies have shown that partial coverage of the radar cell can lead to a decrease in the NRCS, even though partial coverage by breaking waves is significantly larger in the surf zone than in deep water [Lewis and Olin, 1980; Haller and Lyzenga, 2003]. For this reason, we estimate the percentage of the RiverRad radar cell that has a common discrimination tag by taking advantage of the higher resolution of the optical data.



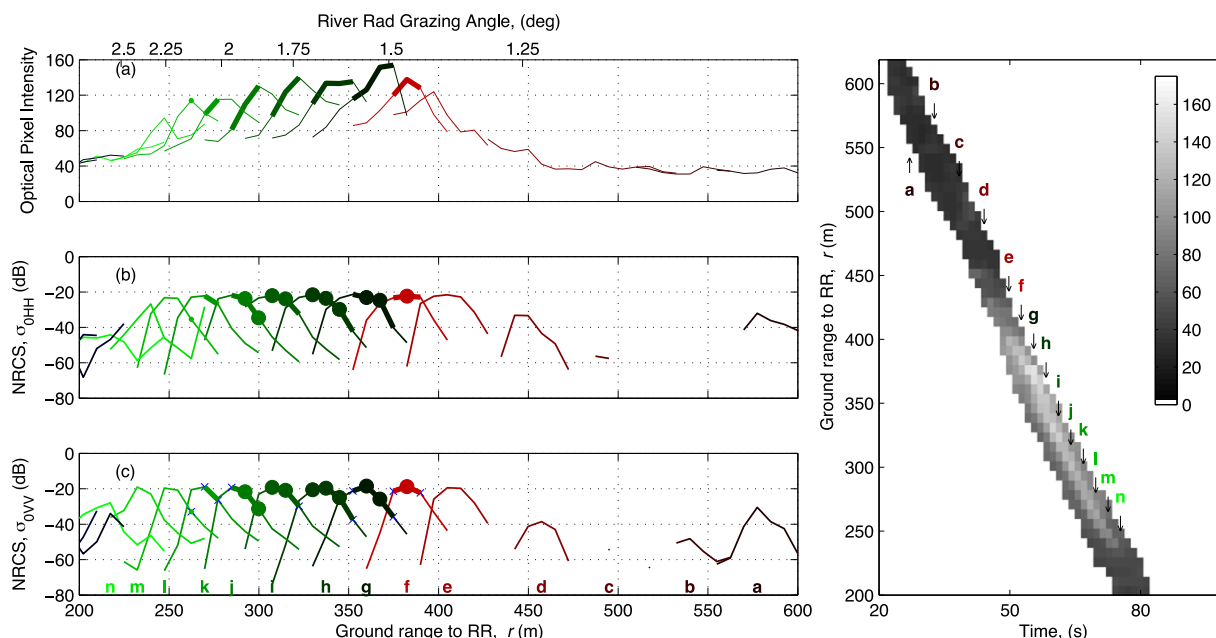


**Figure 5.** Space-time evolution of a wave under energetic conditions at  $\phi \approx 28^\circ$  (collection 23691). (a) Spatial profiles of video intensity tracking the same wave as it propagates, (b) corresponding  $\sigma_{0HH}$  (dB), and (c) corresponding  $\sigma_{0VV}$  (dB). Thicker lines denote sections of the profiles identified as wave breaking where dots indicate data with  $BF_{\text{breaking}} \geq 75\%$ . (right vertical plot) Video time-space map of the event with profiles identified. Gray scale corresponds to the optical pixel intensity.

To do this, each video pixel is assigned a value ( $k = 1, 2, 3$ ) depending on whether it is active breaking, steep waves or remnant foam. Next, the percentage coverage is estimated as:

$$BF_{k^*} = N|_{k=k^*} / N, \quad (2)$$

where  $BF_{k^*}$  is the beam filling fraction of the  $k^*$ th surface type;  $N|_{k=k^*}$  is the number of pixels that satisfy  $k = k^*$  within a given radar cell; and  $N$  is the total number of video pixels within the RiverRad footprint (between 4 and 16 for the ranges used here). As can be seen in the right plots of Figure 4, beam filling factors exceeding 75% are not uncommon. These values are larger than those found by Haller and Lyzenga [2003] at the same coastal site, although in their case for smaller waves in the inner surf zone,  $H_{m0} \approx 0.68$  m. Our results focus on the outer surf zone, where a breaking wave can fill a few consecutive radar cells even at oblique looks (see the cells indicated by white arrows in Figure 1b). Considering that a partial coverage of 75% only reduces the NRCS by about 1 dB, in the following most of the analysis focuses on data satisfying  $BF_{k^*} \geq 0.75$  for all stages, although data with lower values of  $BF_{k^*}$  are retained in some figures for reference.

### 3.2. Backscattered Power and Polarization Ratio

#### 3.2.1. Evolution of Individual Events

We first analyze the scattering characteristics of individual waves as they progress shoreward and evolve through the different stages of the breaking cycle. For each collection, an individual wave is isolated by manually tracking the wavefront in the time-space images such as Figure 4. At each time step, a 52.5 m long window moving with wave is selected to obtain the along-range profile of the signal. In Figure 4 (left plots), selected wave trajectory envelopes are demarcated with white contours, where it can be seen that the selection encompasses shoaling, active breaking, and remnant foam. In Figures 5–7, results are presented for two representative conditions: a higher energy wave climate on 13 May (collection 23691,  $H_{m0} \approx 2.5$  m,  $T_p \approx 11.7$  s), which also exhibits a large amount of remnant foam in the wave troughs; and collections 24863 and 24868 on 15 May, which have clearer signatures of the dark fronts indicative of steepening shoaling waves ( $H_{m0} \approx 1.15$  m,  $T_p \approx 11.6$  s). Results include look directions of  $\phi \approx 2^\circ$  and  $\phi \approx 28^\circ$  relative to the cross-shore axis.

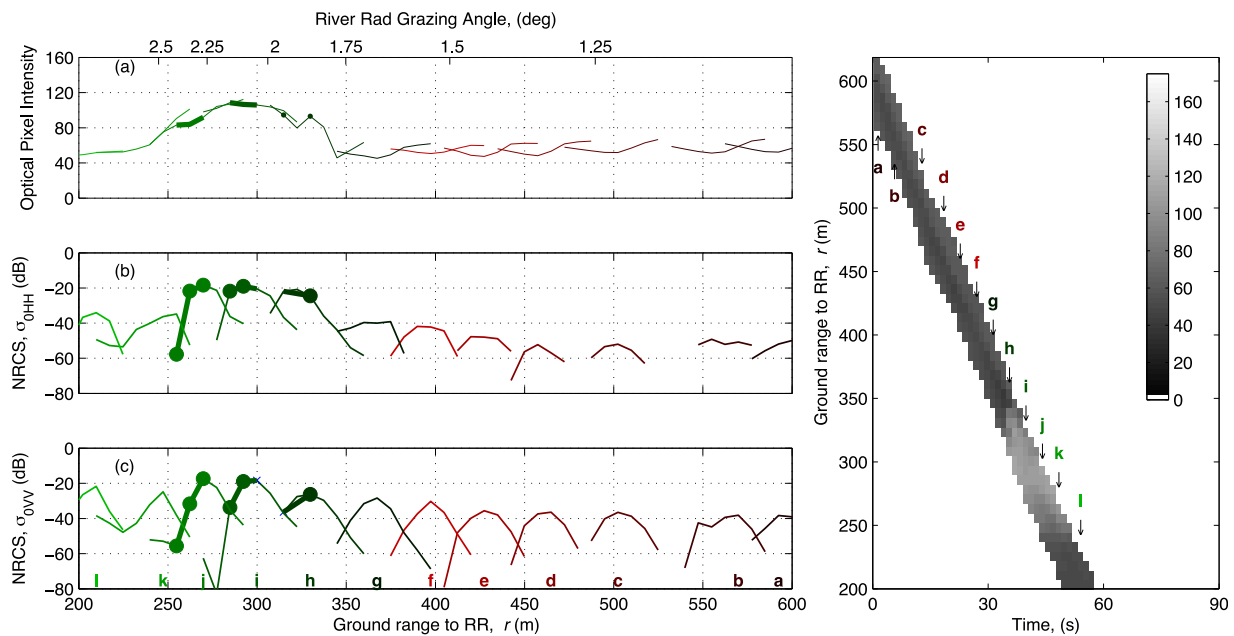


**Figure 6.** Space-time evolution of a shoaling wave for mild wave conditions at  $\phi \approx 28^\circ$  (collection 24863). Same key as Figure 5.

Figure 5 shows range profiles, at different time steps thus moving with the wave, for collection 23691 at  $\phi \approx 28^\circ$ . The rightmost plot shows the optical intensity time-space image, where selected range profiles are marked alphabetically starting from offshore (profile letters also shown at bottom of bottom left plot). The upper left plot shows the optical intensity of these profiles. Instances where active breaking has been identified are highlighted with thicker lines, and locations where  $BF_{\text{breaking}} \geq 0.75$  are marked with large colored dots. The middle plot shows the corresponding backscattered  $\sigma_{0HH}$ , while the bottom plot shows the  $\sigma_{0VV}$ .

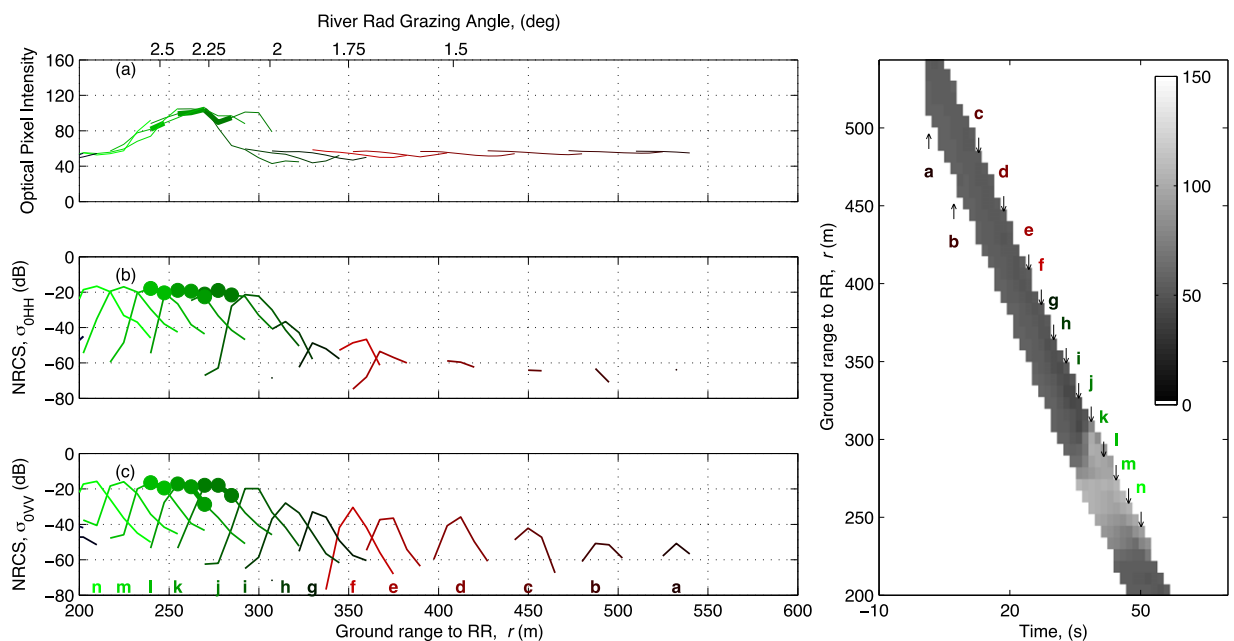


**Figure 7.** Space-time evolution of a shoaling wave for mild wave conditions at  $\phi \approx 2^\circ$  (collection 24868). Same key as Figure 5.

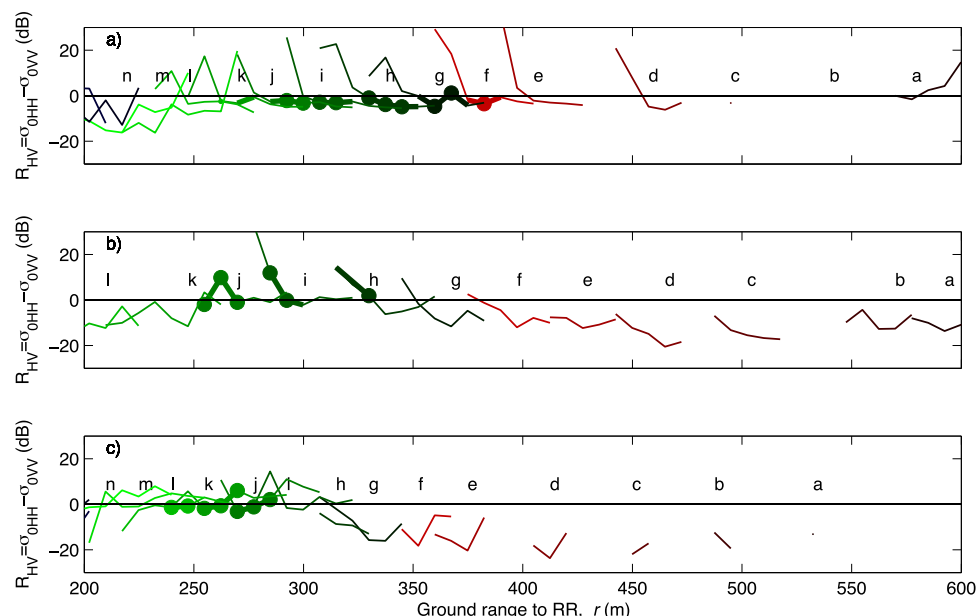


**Figure 8.** Space-time evolution of the polarization ratio for the corresponding profiles of Figures 5–7. Same key as Figure 5. Events with NRCS below the noise level have been removed. (a) Collection 23691, (b) Collection 24863, and (c) Collection 24868.

In both cases, the noise level has been subtracted from the series and data below the noise level are not shown. We can thus follow the time history of the wave and the corresponding changes in the optical and microwave signals. For instance, in the profile marked as *a*, the wave shows an optically dark signature as expected from optical specular scattering from the tilted wavefront. In contrast, the microwave scattering is relatively strong at both polarizations. In this profile, peak NRCS values are aligned with the darker section of the optical data, therefore, the steepest section of the wave. This is consistent with scattering in accordance with the CST. Profiles *b* and *c* keep the low optical levels but show a sudden drop in the backscattered signal, even below the noise level at HH. As the wave continuously evolves, it resumes scattering at larger levels ( $-30$  dB) in *d*, where it can be seen that HH reaches its peak value further shoreward than VV. At *e*, the wave enters the zone of remnant foam from the previous breaker, and then begins to break. There both polarizations show a significant increase in the NRCS and scatter at similar levels (peaking around  $-20$  dB). Throughout the breaking phase of the wave (profiles *f* to *k*), both polarizations scatter at similar levels, and their range-dependent shape is similar, although HH shows a broader peak which spans about 30 m at *f* and decreases to 15 m at *l*. During this time, the optical intensity decays gradually but all these profiles have been classified as breaking events. By profile *m* the wave has ceased breaking and shows a drop in the backscattered power. As the nonbreaking wave progresses through the bar-trough, VV scatters more strongly than HH.

Figure 6 shows profiles for collection 24863 at  $\phi \approx 28^\circ$ , when wave energy and wind speed were moderate. Here a steep shoaling wave is clearly imaged with optically dark front faces correlated with locally increased backscatter until the onset of breaking. It can be seen that during the shoaling phase (profiles *a* through *i*), VV shows larger returns than HH (typically around 20 dB larger) and the peaks at both polarizations align well with the minima in the video signal. As waves move onshore, thus increasing grazing angle, the maxima show a gradual increase, most noticeable at HH. However, the maxima for these steep waves are at least 10 dB less than the maximum values observed for breaking waves (profiles *j* and *k*). During active breaking, the NRCS maxima are similar at both polarizations and comparable to those of the more energetic wave conditions, peaking about  $-20$  dB (collection 23688, cf. Figure 5).

Finally, Figure 7 shows an upwave look ( $\phi \approx 2^\circ$ ) for the same conditions as Figure 6. The evolution is similar to the oblique incidence case, but  $\sigma_{0HH}$  values fall below the noise level during the shoaling phase. In turn,  $\sigma_{0VV}$  profiles are similar to the more oblique cases. Scattering from the active breaking sections of the wave does not indicate a dependence on look angle, peaking again close to  $-20$  dB.

Next, we analyze the polarization ratio, defined as  $R_{HV} = \sigma_{0HH}/\sigma_{0VV}$  ( $\sigma_{0HH} - \sigma_{0VV}$  in dB). According to CST,  $R_{HV}$  should be always less than unity (or 0 dB), and for specular scattering it should be exactly unity. However, previous research has suggested that scattering from breaking waves yields polarization ratios larger than CST predictions and even exceeding unity [e.g., Lewis and Olin, 1980; Kwok and Lake, 1984; Trizna et al., 1991; Lee et al., 1995], and therefore  $R_{HV}$  values in this range have been considered as a wave breaking indicator [Hwang et al., 2008]. However, large polarization ratios have also been associated with steep waves [Liu et al., 1998; West and Ja, 2002] and explained by nonCST scattering mechanisms.

Figure 8 shows the evolution of the polarization ratio for the profiles shown in Figures 5–7. The majority of the nonbreaking profiles show polarization ratios well below 0 dB (e.g., profiles *a* to *f* in Figures 8b and 8c). Polarization ratios of breaking waves in turn concentrate near 0 dB, with an apparent bias toward slightly negative values. The maximum ratios occur at instances shoreward of breaking sections, with large positive values. In general, the increase of  $R_{HV}$  in front of active breaking is very abrupt, typically changing from small negative values to large positive ones over a few radar bins along range. This is consistent with the peak of  $\sigma_{0HH}$  across a breaking wave being more broad in range, as seen in Figures 5–7.

### 3.2.2. Ensemble Results

Results from the wave tracking data suggest that scattering magnitudes from the active breaking section of the waves are distinct from the other stages of the breaking cycle. Next, we assemble the ensemble results from all collections grouped by water surface type. We define an event as the ensemble of connected pixels in the time-space image for a given surface type, at each time step. Results are delivered as a function of the grazing angle measured at the centroid of the event, and are presented in terms of the median NRCS of the group. Typical events gathered up to 5 pixels (i.e., 37.5 m), and the following results consider 2584 breaking events, 305 steep events, and 4890 remnant foam events.

Figure 9 shows the histograms of median NRCS, where the colorscale represents the frequency count at each NRCS-range bin, where the top three rows correspond to breaking waves, steep waves, and remnant foam, respectively. Superimposed on the histograms the median of the median NRCS are shown. These median values are also plotted together on the bottom row for comparison among wave stages. For active breaking events (top), it can be seen that the larger frequency counts concentrate at large NRCS values, peaking near  $-20$  dB. At very low grazing (less than  $1.5^\circ$ ) scattering levels increase rapidly with angle but at larger incidence, the dependency on grazing angle becomes weaker varying just a few dB between  $1.5^\circ$  and  $3.0^\circ$  grazing, where the median NRCS typically exceeds  $-30$  dB.

Figures 9c and 9d show the results for steep waves. These backscatter slightly less strongly than the active breaking waves although can reach large values on occasion. Also,  $\sigma_{0HH}$  shows weaker returns than  $\sigma_{0VV}$ . Finally, in Figures 9e and 9f the data from regions of remnant foam are shown. While significant scatter is present, the median NRCS concentrate about  $-40$  to  $-50$  dB, which is significantly less than those of steep and breaking waves. The median NRCS shows a gradual increase with grazing angle, changing about 20 dB between  $1.0^\circ$  and  $3.5^\circ$  grazing.

In Figure 10, a similar analysis is presented but grouping data by look angle instead. Breakers and foam show no dependency on look angle, and scatter at significantly different levels. Steep waves in turn, show a clearer dependency on look angle, decreasing as the latter increases.

Figure 11 shows results for the median polarization ratio as a function of grazing angle. It can be seen that all wave stages have events exceeding unity (or 0 dB) with some scatter. However, the median of the median polarization ratio shows more gradual trends. Breaking waves have median polarization ratios ranging from 0 to  $-5$  dB, without exhibiting a grazing dependency. Results for steep wave show more scatter although negative median polarization ratios concentrate between 0 and  $-10$  dB. On the other hand, remnant foam shows a distinctive grazing angle dependency, with the median polarization ratio gradually decreasing as the angle increases. By looking at polarization ratios event by event, no clear discrimination of the wave stage can be done with this data set.

The previous results group events just based on viewing geometry. Next, we perform a similar analysis but group the data by environmental parameters, such as wave height and direction, and wind speed and direction (wave period did not vary significantly). In Figure 12, the median NRCS of breaking waves is

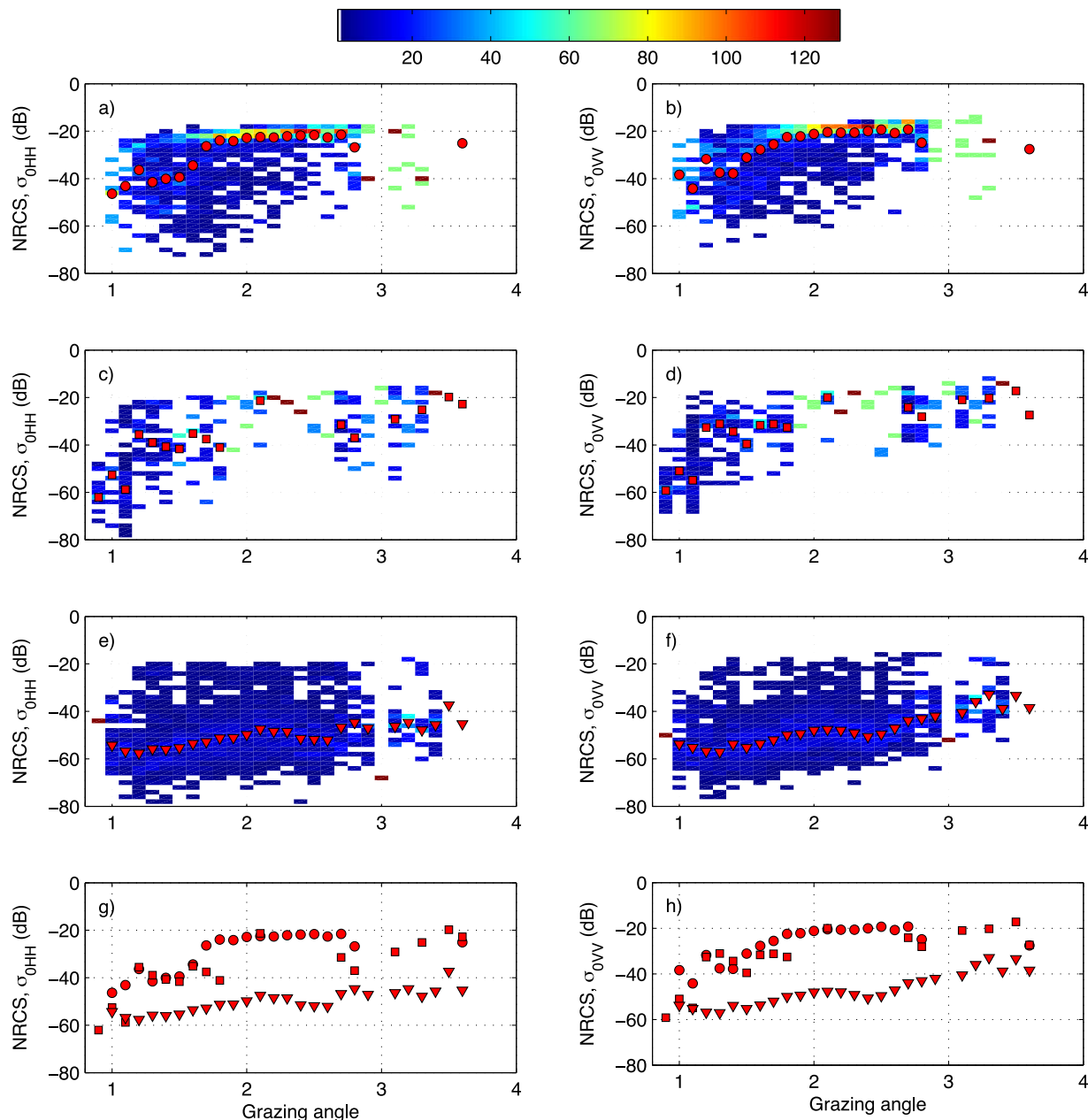


**Figure 9.** Histograms of median NRCS of ensemble events as function of grazing angle for (a and b) breaking, (c and d) steep waves, and (e and f) remnant foam patches. Histograms are calculated at each range bin. (g and h) Red markers are the median NRCS of all events at each range bin for breakers (circles), steep waves (squares), and remnant foam (triangles) which are grouped at the bottom for comparison. Columns correspond to (left)  $\sigma_{0HH}$  and (right)  $\sigma_{0VV}$ .

presented as function of grazing angle and environmental parameters. No dependency on environmental parameters is observed, despite the range of variation found in most of these parameters.

### 3.3. Doppler Spectrum

In addition to the time series of backscattered power, time series of the Doppler offset, Doppler bandwidth and the mean Doppler spectrum (averaged over the 2 min time series) at each range bin were also recorded. These parameters can provide further information regarding the scattering mechanisms and their sources. For example, if pure Bragg scattering was the only mechanism, the mean Doppler spectrum would show a peak at a frequency given by the Bragg resonant condition:



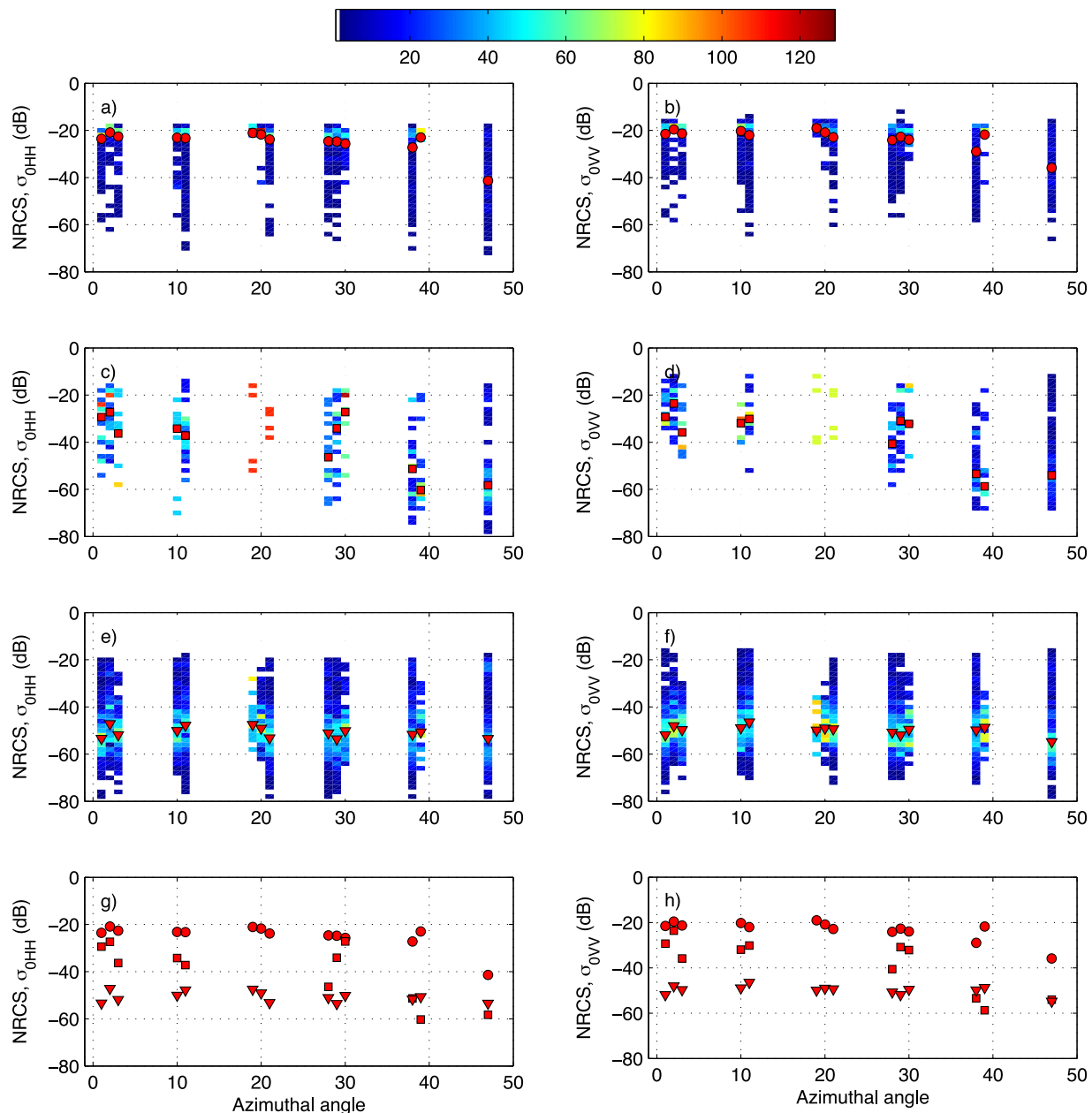


**Figure 10.** Histograms of median NRCS of ensemble events as function of RiverRad look angle. Same key as Figure 9.

$$f_B = \frac{c_B}{\lambda_B} = \frac{2 \sin \theta c_B}{\lambda_0}, \quad (3)$$

where  $f_B$ ,  $\lambda_B$  and  $c_B$  are the frequency, wavelength, and phase speed of the Bragg waves. The latter can be obtained from the deep water dispersion relation.  $\lambda_0$  is the wavelength of the electromagnetic wave ( $\sim 3$  cm at X-band) and  $\theta$  is the incidence angle. In the presence of longer surface gravity waves and/or mean currents, the Doppler peak departs from  $f_B$  as it is modulated by the long wave orbital velocities and/or it is shifted by the mean current. However, in some situations, the Doppler peak is shifted toward even higher frequencies (thus larger scatterer velocities) that correlate well with the phase speed of an underlying long wave [e.g., Lee et al., 1995; Plant, 1997; Farquharson et al., 2005]. These fall outside of traditional

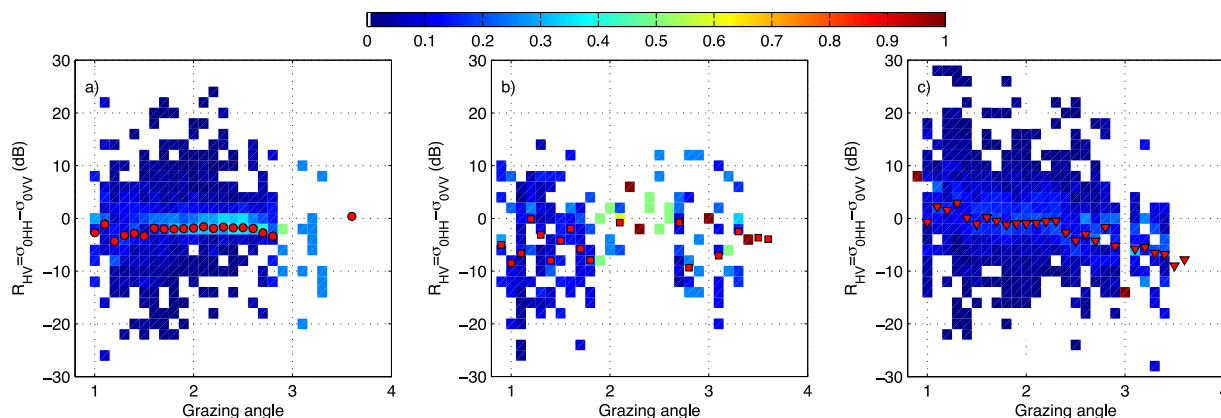


**Figure 11.** Histograms of polarization ratio  $R_{HV}$  of ensemble events as function of grazing angle for (a) breaking, (b), steep waves, and (c) remnant foam patches. Symbols follow the same key as Figure 9.

CST and suggest scattering from sources that are bound to the long waves and can be correlated to, but is not limited to, breaking waves [Lee *et al.*, 1995]. Here we note that the term bound does not refer to the concept of bound waves arising from nonlinear interaction among harmonic frequencies that takes place for shoaling gravity waves, but instead shorter waves riding on top the long wave such as parasitic capillary waves arising from gentle breaking or when waves become steep enough [e.g., Rozenberg *et al.*, 1995; Plant, 1997, 2003].

Figure 13 shows the range evolution of the mean Doppler spectra, where positive frequencies represent scatterers traveling toward the antenna. The leftmost plot is HH Doppler spectra of collection 23691, when several breaking events are present (cf. Figure 4a) whereas the center plots correspond to the HH and VV Doppler spectra for collection 24868 when only one breaking event was detected (cf. Figure 4e). The vertical white line denotes ranges where at least one breaking event was detected during the 2 min window. Finally, plots (d)–(g) show the spectra at selected ranges, indicated by the white arrows in plots (a)–(c). It can be seen that for the lower wave energy case (collection 24868, middle plots) the spectra show a distinct behavior between locations where at least one breaking event was present and those where no breaking occurs. For nonbreaking waves, the spectra show energy concentrated within a narrow range of frequencies close to the Bragg frequency as indicated by the down-arrows in plots (d)–(g), with a clear bias toward positive frequencies, thus scatterers traveling toward the radar. See for example the thick lines corresponding to collection 24868 in plot (d),  $r = 525$  m. As the wave shoals, the spectra at both polarizations broaden slightly but, as observed by Lee *et al.* [1995], VV retains a local peak near the Bragg frequency, which is significantly weaker in magnitude at HH (e.g., thick lines in Figure 13f at  $r = 350$  m). However, if the record contains at least one breaking event, the distinction becomes negligible, both spectra become significantly broader and peak at higher frequencies (e.g., spectra at  $r = 250$  m, roughly corresponding to  $x = 300$  m). The spectra when waves are breaking show no clear polarization dependence (see thin lines in plots (e) and (f)) and are nearly identical for both collections (plot (g)), despite the different number of breaking events present. Moreover, in Figure 14 an estimation of the variability in Doppler spectra at this location for 14 collections whose look angle was below  $\phi < 15^\circ$  is presented, where shaded areas correspond to data within one standard deviation from the mean. Again, variability between HH and VV data is negligible, but it is remarkable the small degree of variability among these 14 runs as indicated by the small standard deviation, despite them being collected for a range of environmental conditions. The number of breaking events at this location varied between 1 and 6 events, indicating that one event suffices to dominate the spectra. In addition, the spectral peak is narrow, indicating that the main scatterers travel at roughly the same speed for all these collections.

However, the first plot of Figure 13 shows that the spectra also are subject to broadening at locations where breaking was not identified. However, at these locations very steep waves were identified (see Figure 4a) indicating waves initiating the breaking process. We will discuss this in the following sections.

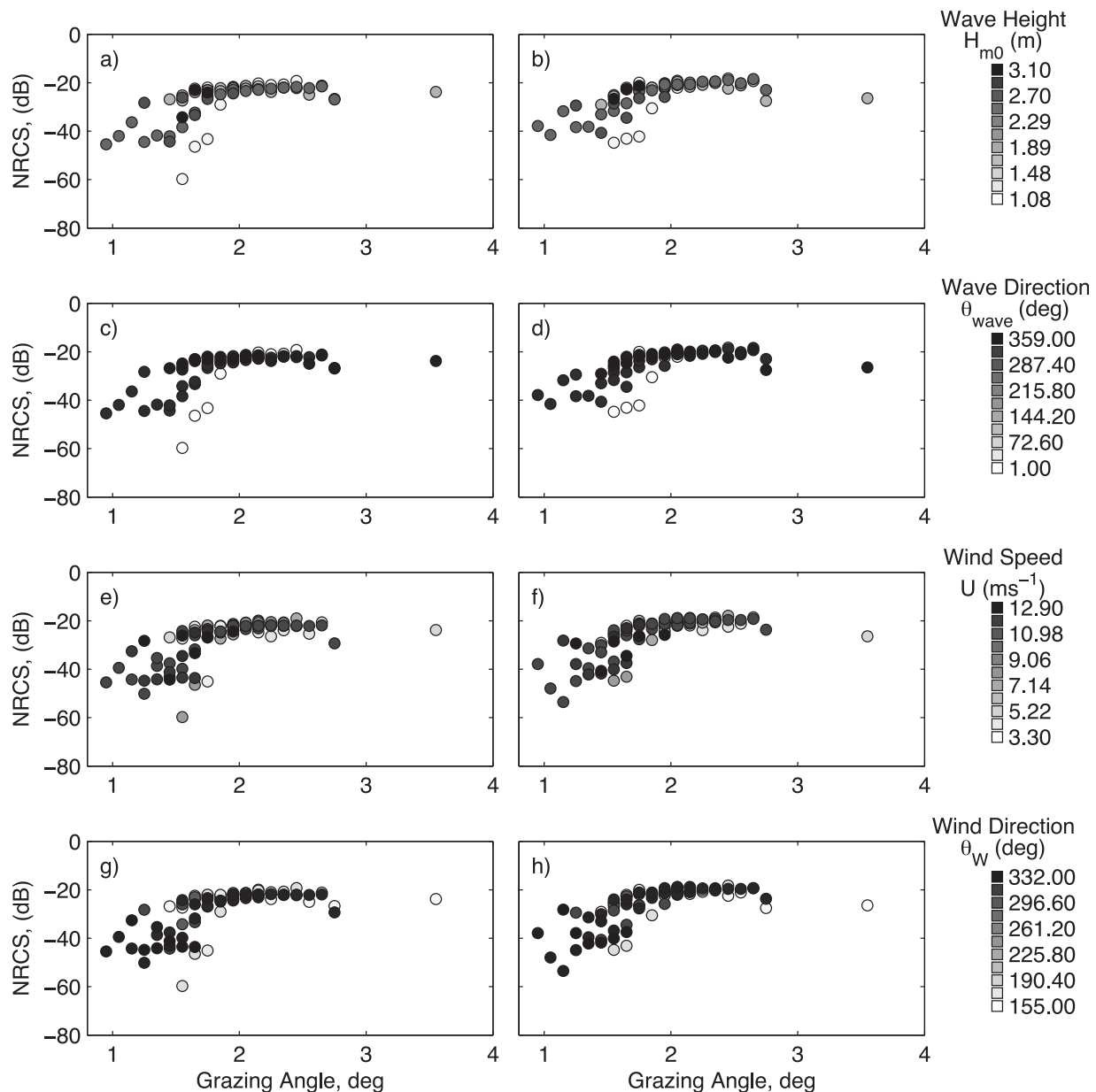


**Figure 12.** Median NRCS of breaking waves classified by environmental parameters magnitude. Rows correspond to significant wave height  $H_{m0}$ , mean wave direction, wind speed, and wind direction, respectively. Columns correspond to (left)  $\sigma_{0HH}$  and (right)  $\sigma_{0VV}$ .

### 3.4. Doppler Offset

Finally, we analyze the Doppler offset  $f_D$ , which corresponds to the frequency of the Doppler spectral peak at each time and range bin. Although the information at frequencies other than the spectral peak is discarded, the analysis of this quantity can be related to the mean radial surface velocity of the dominant scatterers,  $V$ , by [e.g., *Plant et al.*, 2005]:

$$V = \frac{f_D \lambda_0}{2 \sin \theta}, \quad (4)$$

thus allowing the analysis of its time and space evolution at high resolution. Time-space maps of the along-range surface velocity are shown in Figure 15 (collection 23691, energetic wave conditions) and Figure 16 (collection 24868, milder wave conditions), where thin black contours indicate breaking waves. Both time-

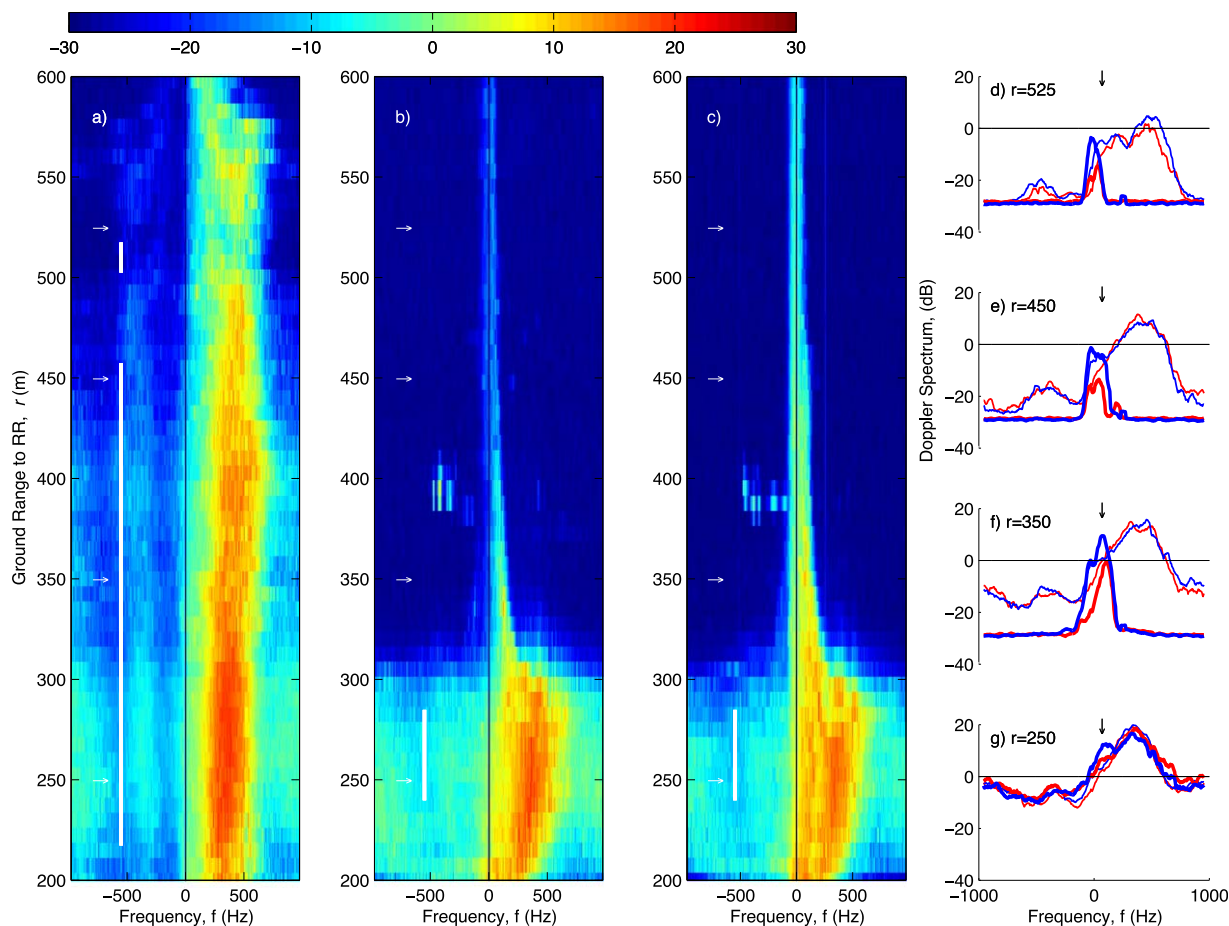


**Figure 13.** Mean Doppler spectra, dB. (a) Collection 23691 at HH, (b) HH, and (c) VV for collection 24868, where white line indicates ranges where at least one breaking event was detected. (d–g) Plots of mean Doppler spectra at ranges indicated by white arrows in plots (a–c). Blue lines correspond to VV and red lines to HH. Thicker lines correspond to collection 24868. Black arrows indicate the Bragg frequency.

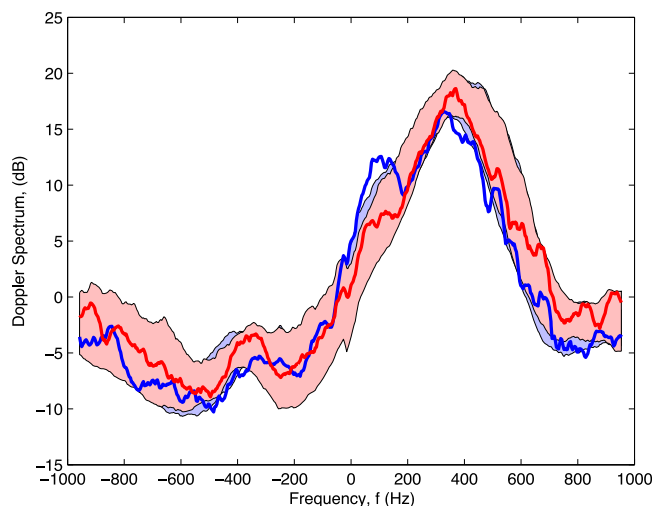


**Figure 14.** Doppler spectra variability at  $r = 250$  m, for collections where  $\phi < 15^\circ$ . Shaded areas correspond to data within one standard deviation from the mean, mean not shown. Lines correspond to spectra of collection 24868 (see Figure 13) for reference. Blue is VV and red is HH.

space maps clearly show the presence of propagating waves, especially for the more energetic wave conditions when wave tracks can be seen at all ranges. When waves are smaller, tracks are more discernible at VV than HH as expected from CST. Negative velocities (moving away from the antenna) are observed in the wave troughs, but are more evident for the milder wave conditions. Their absolute magnitude is significantly smaller than the magnitudes observed near wavefronts and crests. Regardless of environmental conditions, active breaking exhibits large velocities that decay as the waves progress onshore.



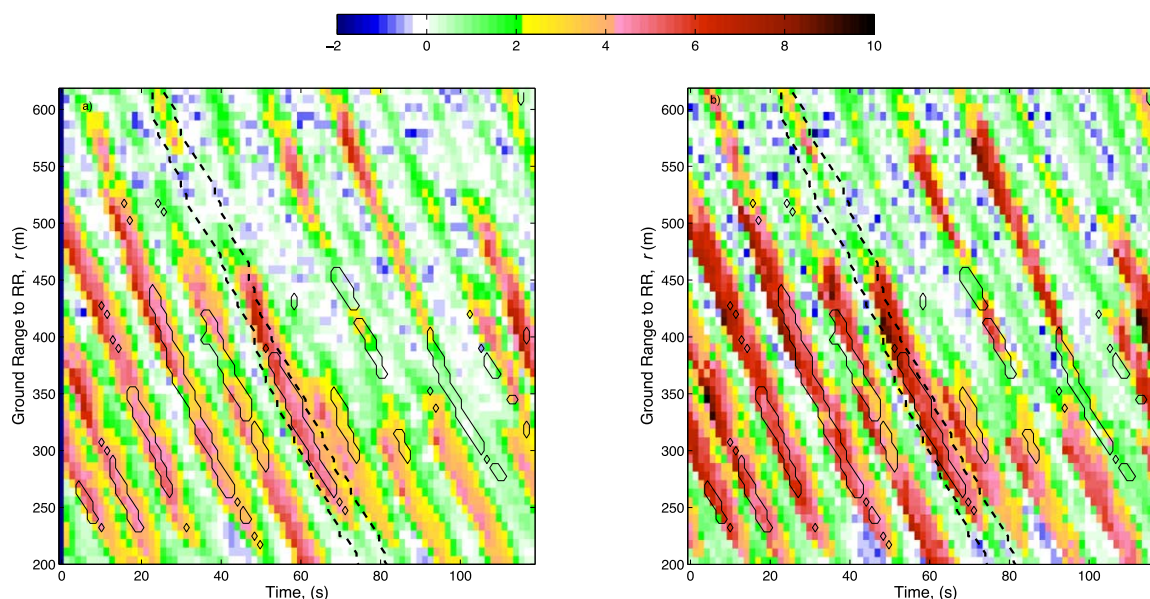


**Figure 15.** Time-space maps of surface radial velocities (m/s) derived from the Doppler offset, for collection 23691. (a) HH and (b) VV. Thin contours denote locations identified as breaking, and dashed contours correspond to the individual wave identified in section 3.2.1.

Figure 17 shows the profiles of the surface velocities, derived from the Doppler offset, of the individual wave events identified in section 3.2.1. The surface velocities associated with breaking events are much larger than those of nonbreaking events. The surface velocity of the active breaking waves exceed 5 m/s and do not show a clear distinction between polarizations nor different environmental conditions. The range profiles of the surface velocity at each time step show a peak in velocity magnitude. Nonbreaking waves in turn show smaller surface velocities in the shoaling region, usually not exceeding 2 m/s.

In summary, observation of a suite of radar backscattering parameters have been presented for the different stages of the nearshore wave breaking cycle, with a special emphasis on the scattering from surf zone breaking waves. While most of the results are consistent in some aspects with previous observations, certain specific details are worth to be highlighted. We will discuss them in the following sections.

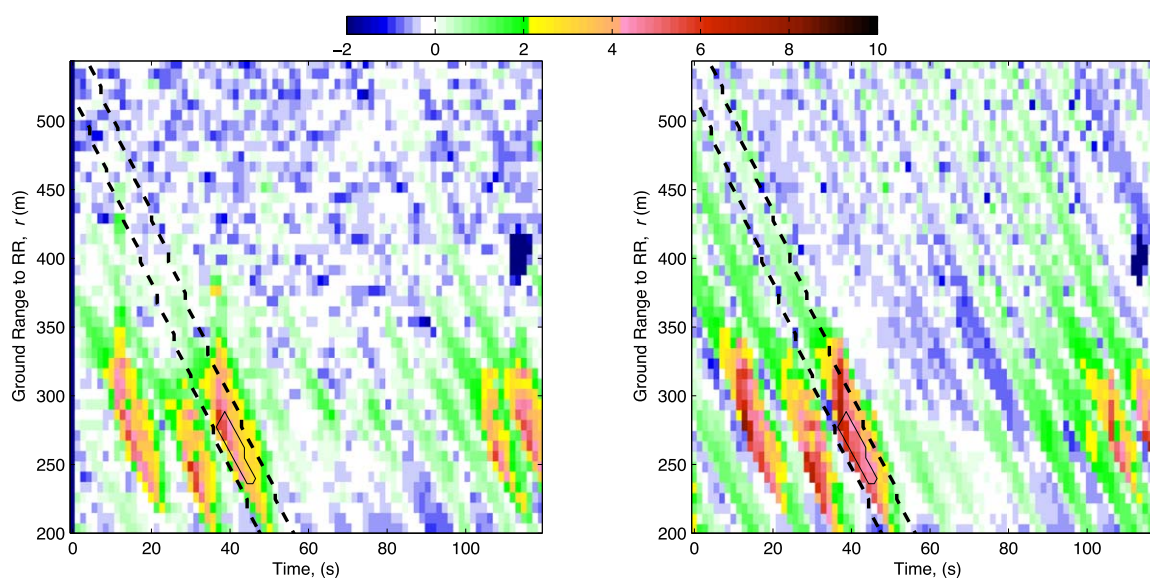


**Figure 16.** Time-space maps of surface radial velocities (m/s) derived from the Doppler offset, for collection 23868. Same key as Figure 15.



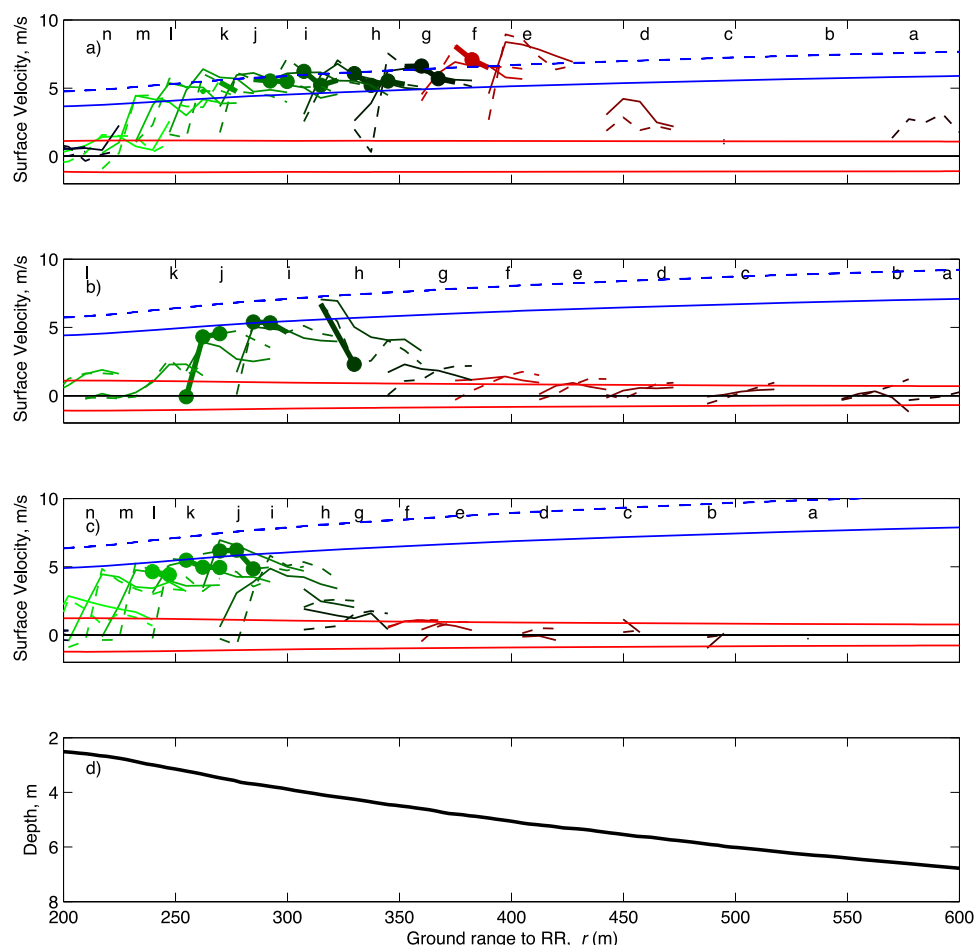


**Figure 17.** Space-time evolution of the surface radial velocity for the corresponding profiles of Figures 5–7. Similar key as Figure 5, plus solid blue lines corresponding to the modeled phase speed  $c$  of a linear wave, dashed blue lines correspond to  $1.3c$ , and red lines correspond to the orbital velocity extrema. Solid surface radial velocity lines are HH records, and dashed lines correspond to VV data. (a) Collection 23691, (b) Collection 24863, (c) Collection 24868, and (d) Bathymetric profile (December 2007).

#### 4. Discussion

In this section, we will discuss the ramifications of some of the results from this study and place those results in context with previous work. First, we note that previous studies have attempted to define the characteristics of microwave scattering from breaking waves in order to use radar observations for wave breaking detection. One potentially detectable characteristic is the presence of high polarization ratios [Hwang *et al.*, 2008]. In the present work, we were able to examine the polarization ratios along individual wave profiles and to spatially correlate the observed high polarization ratios ( $R_{HV} > 0$ ) to the portion of the front face of the wave that leads the active breaking region, which is consistent with models for multipath scattering. Moreover, the active breaking portion yields polarization ratios of ( $R_{HV} \sim 0$ ). Models for the source of multipath reflections include: bulges and plumes [Wetzel, 1986, 1990], water dihedrals [Trizna, 1997; Plant *et al.*, 2010], and the shape of the water surface near breaking [e.g., Lewis and Olin, 1980; West, 1999; Fuchs *et al.*, 1999; Sletten *et al.*, 2002; Melief *et al.*, 2006; Li and West, 2006]. Hence, while multipath scattering (and high polarization ratios) can be associated with the shape of waves that are breaking, they are not inherent properties of the active breaking region where most of the wave dissipation is occurring. In addition, our results indicate that steep waves and remnant foam can also induce large polarization ratios, which further complicates the association of high polarization ratios with active wave breaking.

A second known characteristic of the scattering from breaking waves is that the mean Doppler spectrum is subject to broadening and bias to higher frequencies by sporadic, but large power, scattering events. The Doppler peak is shifted to high frequencies by scattering arising from the active breaking portion of the wave [e.g., Smith *et al.*, 1996] with spectral broadening being driven by surface disturbances produced on the

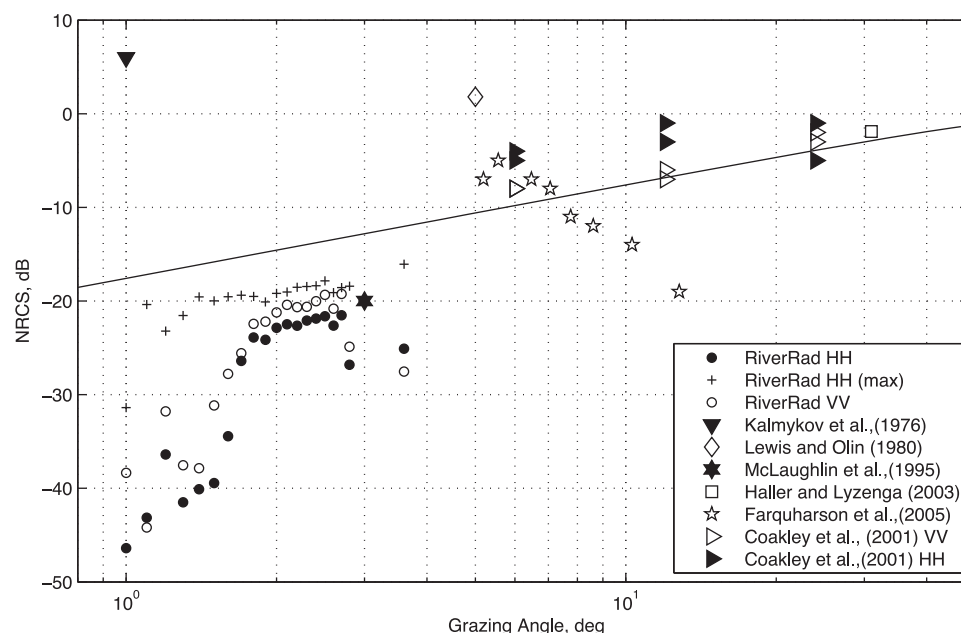


**Figure 18.** Grazing angle dependency of NRCS from various data sets. Line corresponds to grazing angle dependency of a Lambertian scattering surface.

turbulent front face that have a range of speeds about their spatial mean, which is the local wave celerity [e.g., *Fuchs et al.*, 1999; *Coakley et al.*, 2001; *Farquharson et al.*, 2005]. All locations where breaking waves were identified, this shift and broadening were identified in the Doppler spectra. Herein, we have shown that for surf zone waves the presence of even just one breaking event (during a 2 min record) is sufficient to fundamentally change the mean Doppler spectrum. Moreover, we have found that the spectra at locations where breaking was persistent among different collections showed little variability, also indicating that the scattering characteristics do not depend on environmental parameters for breaking waves.

However, it is also known that small-scale bound waves can also lead to spectral broadening and peak frequency shifting toward high frequencies, as shown for different microwave frequencies and incidence angles by *Rozenberg et al.* [1995, 1996]; *Plant* [1997, 2003], among others. We also found evidence of spectral broadening at locations where breaking was not identified, although steepening waves were found on occasion at these locations. Even though they worked at a different frequency and grazing angle, *Jessup et al.* [1991] considered the spectral broadening as a breaking indicator, but they considered as breakers waves whose breaking onset was up to 20% of the wavelength downwave. For our results, the broadening takes place up to one wavelength upwave of the breaking onset (see Figure 13), preventing considering them as an active breaking wave and complicating the use of spectral broadening as a breaking indicator.

It is also of interest to investigate whether the time varying, line of sight Doppler velocity (corresponding to the peak in the Doppler spectrum) can be related to the local wave height. For nonbreaking waves, and in the absence of strong winds, the oscillations in the Doppler velocity about the Bragg peak should represent the surface orbital velocity of the incoming waves. This is potentially a useful tool for the remote measurement of surface displacements and/or wave height [*Nwogu and Lyzenga*, 2010]. However, our results indicate that such a methodology will require extreme care for systems operating in the nearshore at low grazing angles. Specifically in Figure 17, we compare the observed Doppler velocities with estimates of the local wave surface orbital velocity amplitude  $u_m$  and the local wave celerity  $c$  computed from linear wave theory by:

$$c = \sqrt{\frac{g}{k} \tanh(kh)}, \quad (5)$$

$$u_m = \frac{H}{2} \frac{2\pi \cosh(kh)}{T_p \sinh(kh)}, \quad (6)$$

where  $h$  is the local water depth, and  $T_p$ ,  $k$ , and  $H$  are the gravity wave period, wavenumber, and height, respectively. Although nonlinear effects can affect the phase speed  $c$  by more than 10% in the surf zone [e.g., Catalán and Haller, 2008], we use the linear dispersion model as a first step in the comparison. We note the use of only  $u_m$  as waves were approximately shore-normal. The best estimate we have for the bathymetry during the experiment is the data collected the previous winter (December 2007), which we used in the calculation of  $c$  and  $u_m$ . This bathymetry showed nearly alongshore uniform profiles, with an off-shore bar near  $x = 400$  m in the FRF system, and is qualitatively similar to the conditions present in this study. The surface orbital velocity amplitude is also dependent on the local wave height, which was estimated using the Thornton and Guza [1983] wave transformation model initialized with data from the FRF 8m array. The line of sight velocity was then calculated by multiplying by  $\cos\phi$ . The results are presented in blue ( $c$ , solid;  $1.3 c$ , dashed) and red lines ( $\pm u_m$ ) shown in Figure 17.

The model-data comparison shows that the observed surface velocities correlate fairly well with the estimated surface orbital velocity for nonbreaking waves and with the estimated wave celerity for breaking waves. However, for the nonbreaking waves it appears only the positive shoreward velocities at the wave crests are well captured and the velocities in the wave troughs are near 0 m/s, which is likely an underestimate of their magnitude. More importantly, the transition of the Doppler velocities from their correspondence to orbital velocities to wave celerity instead, takes place over short cross-shore distances. Hence, relating the observed velocities to wave characteristics will require specific knowledge of the time-space variability of wave breaking.

Finally, it was found that the backscattering from the active breaking portion of the wave can reach similar scattering levels at both polarizations and is generally insensitive to wave and wind conditions, and azimuthal angle. Median NRCS values were close to  $-20$  dB, while showing a positive dependency on grazing angle. These NRCS levels are larger than those predicted by CST, and also larger by a few dB than the scattering from other scattering sources as observed herein, but are generally lower than previous observations in the surf zone. However, it must be noted that the present data have been obtained at lower grazing angles (less than  $3.5^\circ$ ). To put the data in context, a summary of previous nearshore observations and the present data set are presented in Figure 18 [Kalmykov *et al.*, 1976; Lewis and Olin, 1980; Haller and Lyzenga, 2003; Farquharson *et al.*, 2005]. We have also included one laboratory data set by [Coakley *et al.*, 2001], and data taken at  $3^\circ$  grazing by McLaughlin *et al.* [1995], although for very short waves, thus steepness limited, in a nearshore setting. It is worth noting that these previously reported values correspond to peak NRCS, whereas our data has been presented in terms of median NRCS. For this reason, the HH NRCS maxima have also been included for reference. While our data are indeed a few dB lower than other surf zone data, they compare favorably with data from [McLaughlin *et al.*, 1995] taken at similar grazing angles. Moreover, if all data are considered in unison, a positive grazing angle dependency trend is apparent. The exceptions are the data by Kalmykov *et al.* [1976], which exceeds significantly the values observed here at similar grazing angles. Although, we note that those data were collected as waves broke over a breakwater, and were challenged to explain the scattering mechanism responsible for such high NRCS values.

Therefore, we consider the present scattering levels from breaking waves to be in accordance with previously reported data. Moreover, it is indicative that the overall scattering from the active breaking portion of the wave shows a clear dependency on grazing angle, but no polarization dependency. While it is accepted that several scattering mechanisms can coexist during the breaking cycle studied here, the obvious source of scattering from the active breaking portion is that of a very rough surface [Kalmykov *et al.*, 1976; Lewis and Olin, 1980; Coakley *et al.*, 2001], which is generated mechanically by the breaking process. Its NRCS is not directly dependent on environmental conditions and can yield similar scattering levels for both polarizations, hence, polarization ratios close to unity. Recently, Hwang *et al.* [2013] found that temporal decorrelation of breaking waves was consistent with that of a very rough surface, and could be used as wave breaking discriminator for InSAR imagery. Despite the obviousness of the rough surface assumption, no specific model exists to predict the nature of the rough surface or the apparent independence from environmental parameters found here. Lewis and Olin [1980] and Coakley *et al.* [2001] succinctly suggest it is a Lambertian scatterer, for which case the incident angle dependency should follow a cosine law. In Figure 18, the  $\cos\theta$  (in dB, when compared against normal incidence) expected rate of decay of a Lambertian scatterer has been superimposed on the data. It can be seen that an overall good agreement on the trend is obtained despite the scatter of about  $\pm 10$  dB from individual data sets.

## 5. Conclusions

In this work, we have investigated the scattering characteristics of waves as they undergo the different stages of the depth-limited breaking cycle in the surf zone. Our experimental setting allowed measurements at lower grazing angles than previously reported. The use of an automated, independent discrimination algorithm allowed the study of a larger number of events than previous nearshore studies. A suite of microwave parameters was analyzed, including the backscattered NRCS, polarization ratios, and Doppler spectra. While most of the observations are consistent in one way or another with prior research at low grazing angles, the most outstanding results are those regarding scattering from the active breaking portion of the wave, where both polarizations present sustained levels of relatively large and nearly identical scattered power yielding median polarization ratios slightly less than unity. No dependency on look angle or environmental parameters was found for active breaking. Median NRCS are slightly larger than those of steepening waves, yet lower than those observed at slightly higher grazing angles by previous research. However, a positive dependency on grazing angle which correlates well with existing data was found. In addition, active breaking clearly broadens the Doppler spectrum, and a single breaking event suffices to induce this broadening. This means that the Doppler spectrum is highly sensitive to the large power of breaking events. In turn, the Doppler speeds of breaking waves are due to a population of energetic scatterers traveling with the carrier wave. These results were found to be consistent with scattering from a very rough surface that is being mechanically generated by the breaking process, with a similar grazing angle dependency of a Lambertian scatterer.

Finally, we observed that steep waves and remnant foam can reach large backscattered power on occasion, but typically scatter at least 5–15 dB less than breaking. Their VV returns are usually larger than HH, and their Doppler velocity correlates well with the wave orbital velocity. For all wave stages, the polarization ratio exhibits a large amount of variability and values exceeding unity, making this parameter unreliable as discriminator of wave breaking. Instead, high polarization ratios are found on the shoreward edge of the active breaking waves, indicating two distinct scattering regimes. The use of other microwave parameters also points to different stages of the wave cycle yielding similar scattering characteristics as active breaking on occasion. Consequently, if used independently, they would be unreliable discriminators, highlighting the challenges in identifying breaking waves on microwave data alone. This further emphasizes the benefits that sensor fusion techniques as the one used here can have for nearshore remote sensing.

## Acknowledgments

The authors would like to thank Dennis Trizna (Imaging Science Research, Inc.), the staff of the USACE Field Research Facility, Rob Holman and John Stanley (Coastal Imaging Lab, OSU) and Gene Chatham (APL-UW) for their support and contributions during the field experiment. We also would like to thank the three anonymous reviewers for their helpful comments that led to an improved paper. This work was supported by the Office of Naval Research under awards N00014-06-1-0317, N00014-08-1-0636, and N00014-10-10318. P.A. Catalán also thanks CONICYT through its grants FONDECYT 1120878, FONDAPE 15 11-0017, and CCTVAL-FB0821. Data used for producing the results herein may be requested by contacting the authors.

## References

- Bass, F. G., I. M. Fuks, A. I. Kalmykov, I. E. Ostrovsky, and A. D. Rosenberg (1968), Very high frequency radio scattering by a disturbed sea surface: 2. Scattering from an actual sea surface, *IEEE Trans. Antennas Propag.*, AP-16, 560–568.
- Bell, P. S. (1999), Shallow water bathymetry derived from an analysis of X-band marine radar images, *Coastal Eng.*, 37, 513–527, doi:10.1016/S0378-3839(99)00041-1.
- Catalán, P., and M. Haller (2008), Remote sensing of breaking wave phase speeds with application to nonlinear depth inversion, *Coastal Eng.*, 55, 93–111, doi:10.1016/j.coastaleng.2007.09.010.
- Catalán, P. A., M. C. Haller, R. A. Holman, and W. J. Plant (2011), Optical and microwave detection of surf zone breaking waves, *IEEE Trans. Geosci. Remote Sens.*, 49(6), 1879–1893, doi:10.1109/TGRS.2010.2095864.
- Coakley, D. B., P. M. Haldeman, D. G. Morgan, K. R. Nicolas, D. R. Penndorf, L. B. Wetzel, and C. S. Weller (2001), Electromagnetic scattering from large steady breaking waves, *Exp. Fluids*, 30(5), 479–487, doi:10.1007/s003480000220.
- Dankert, H., and W. Rosenthal (2004), Ocean surface determination from X-Band radar-image sequences, *J. Geophys. Res.*, 109, C04016, doi:10.1029/2003JC002130.
- Farquharson, G., S. J. Frasier, B. Raubenheimer, and S. Elgar (2005), Microwave radar cross sections and Doppler velocities measured in the surf zones, *J. Geophys. Res.*, 110, C12024, doi:10.1029/2005JC003022.
- Flampouris, S., F. Ziemer, and J. Seemann (2008), Accuracy of bathymetric assessment by locally analyzing radar ocean wave imagery (February 2008), *IEEE Trans. Geosci. Remote Sens.*, 46(10), 2906–2913, doi:10.1109/TGRS.2008.919687.
- Frasier, S. J., Y. Liu, D. Moller, R. E. McIntosh, and C. Long (1995), Directional ocean wave measurements in a coastal setting using a focused array imaging radar, *IEEE Trans. Geosci. Remote Sens.*, 33(2), 428–440, doi:10.1109/36.377943.
- Frasier, S. J., Y. Liu, and R. E. McIntosh (1998), Space-time properties of radar sea spikes and their relation to wind and wave conditions, *J. Geophys. Res.*, 103, 18,745–18,757, doi:10.1029/98JC01456.
- Fuchs, J., D. Regas, T. Waseda, S. Welch, and M. P. Tulin (1999), Correlation of hydrodynamic features with LGA radar backscatter from breaking waves, *IEEE Trans. Geosci. Remote Sens.*, 37(5), 2442–2460, doi:10.1109/36.789641.
- Haller, M. C., and D. R. Lyzenga (2003), Comparison of radar and video observations of shallow water breaking waves, *IEEE Trans. Geosci. Remote Sens.*, 41(4), 832–844, doi:10.1109/TGRS.2003.810695.
- Haller, M. C., D. Honegger, and P. A. Catalan (2014), Rip current observations via marine radar, *J. Waterw. Port Coastal Ocean Eng.*, 140(2), 115–124, doi:10.1061/(ASCE)WW.1943-5460.0000229.
- Hasan, G. M. J., and S. Takewaka (2009), Wave run-up analyses under dissipative condition using x-band radar, *Coastal Eng. J.*, 51(02), 177–204, doi:10.1142/S0578563409001990.

- Holman, R., and M. C. Haller (2013), Remote sensing of the nearshore, *Annu. Rev. Mar. Sci.*, 5(1), 95–113, doi:10.1146/annurev-marine-121211-172408.
- Holman, R., and J. Stanley (2007), The history and technical capabilities of Argus, *Coastal Eng.*, 54, 477–491, doi:10.1016/j.coastaleng.2007.01.003.
- Hwang, P. A., M. A. Sletten, and J. V. Toporkov (2008), Analysis of radar sea return for breaking wave investigation, *J. Geophys. Res.*, 113, C02003, doi:10.1029/2007JC004319.
- Hwang, P. A., J. V. Toporkov, M. A. Sletten, and S. P. Menk (2013), Mapping surface currents and waves with interferometric synthetic aperture radar in coastal waters: Observations of wave breaking in swell-dominant conditions, *J. Phys. Oceanogr.*, 43, 563–582, doi:10.1175/JPO-D-12-0128.1.
- Izquierdo, P., and C. Guedes Soares (2005), Analysis of sea waves and wind from X-band radar, *Ocean Eng.*, 32, 1404–1419, doi:10.1016/j.oceaneng.2004.11.05.
- Jähne, B., J. Klink, and S. Waas (1994), Imaging of short ocean wind waves: A critical theoretical review, *J. Opt. Soc. Am. A Opt. Image Sci.*, 11(8), 2197–2209, doi:10.1364/JOSAA.11.002197.
- Jessup, A. T., W. K. Melville, and W. C. Keller (1991), Breaking waves affecting microwave backscatter: 1. Detection and verification, *J. Geophys. Res.*, 96, 20,547–20,559.
- Kalmykov, A. I., and V. V. Pustovoytenko (1976), On polarization features of radio signals scattered from the sea at small grazing angles, *J. Geophys. Res.*, 81, 1960–1964.
- Kalmykov, A. I., A. S. Kurekin, Y. A. Lementa, I. E. Ostrovskii, and V. V. Pustovoytenko (1976), Characteristics of SFH scattering at breaking sea waves, *Radiophys. Quantum Electron.*, 19(9), 923–928, doi:10.1007/BF01044049.
- Kwoh, D. S. W., and B. M. Lake (1984), A deterministic, coherent, and dual-polarized laboratory study of microwave backscattering from water waves. Part I: Short gravity waves without wind, *IEEE J. Oceanic Eng.*, 9(5), 291–308.
- Lee, P. H., J. D. Barter, K. L. Beach, C. L. Hindman, B. M. Lake, H. Rungaldier, J. C. Shelton, A. B. Williams, and H. C. Yuan (1995), X band microwave backscattering from ocean waves, *J. Geophys. Res.*, 100, 2591–2611, doi:10.1029/94JC02741.
- Lewis, B. L., and I. D. Olin (1980), Experimental study and theoretical model of high-resolution radar backscatter from sea surfaces, *Radio Sci.*, 15(4), 815–828.
- Li, Y., and J. West (2006), Low-grazing-angle scattering from 3-D breaking water wave crests, *IEEE Trans. Geosci. Remote Sens.*, 44(8), 2093–2101, doi:10.1109/TGRS.2006.872129.
- Liu, Y., S. Frasier, and R. McIntosh (1998), Measurement and classification of low grazing angle radar sea spikes, *IEEE Trans. Antennas Propag.*, 46(1), 27–40, doi:10.1109/8.655448.
- Lyzenga, D. R., A. L. Maffet, and R. A. Shuchman (1983), The contribution of wedge scattering to the radar cross section of the ocean surface, *IEEE Trans. Geosci. Remote Sens.*, 31, 502–505.
- McLaughlin, D. J., N. Allan, E. M. Twarog, and D. B. Trizna (1995), High resolution and polarimetric radar and scattering and measurements of low and grazing angle and sea clutter, *IEEE J. Oceanic Eng.*, 20(3), 166–178, doi:10.1109/48.393072.
- McNinch, J. E. (2007), Bar and Swath Imaging Radar BASIR: A mobile X-band radar designed for mapping nearshore sand bars and swash-defined shorelines over large distances, *J. Coastal Res.*, 23(1), 59–74, doi:10.2112/05-0452.1.
- Melief, H. W., H. Greidanus, P. van Genderen, and P. Hoogeboom (2006), Analysis of sea spikes in radar sea clutter data, *IEEE Trans. Geosci. Remote Sens.*, 44(4), 985–993, doi:10.1109/TGRS.2005.862497.
- Nieto Borge, J. C., K. Reichert, and J. Dittmer (1999), Use of nautical radar as wave monitoring instrument, *Coastal Eng.*, 37, 331–342, doi:10.1016/S0378-3839(99)00032-0.
- Nwogu, O. G., and D. R. Lyzenga (2010), Surface-wavefield estimation from coherent marine radars, *IEEE Geosci. Remote Sens. Lett.*, 7(4), 631–635, doi:10.1109/LGRS.2010.2043712.
- Perkovic, D., T. C. Lippmann, and S. J. Frasier (2009), Longshore surface currents measured by Doppler radar and video PIV techniques, *IEEE Trans. Geosci. Remote Sens.*, 47(8), 2787–2800, doi:10.1109/TGRS.2009.2016556.
- Phillips, O. (1988), Radar returns from the sea surface: Bragg scattering and breaking waves, *J. Phys. Oceanogr.*, 18(8), 1065–1074, doi:10.1175/1520-0485(1988)018<1065:RRFTSS>2.0.CO;2.
- Plant, W. J. (1990), Bragg sea scattering of electromagnetic waves from the air/sea interface, in *Surface Waves and Fluxes*, vol. 2, edited by G. L. Gernaert and W. J. Plant, chap. 11, pp. 41–108, Kluwer Acad., Springer, Netherlands.
- Plant, W. J. (1997), A model for microwave Doppler sea return at high incidence angles: Bragg scattering from bound, tilted waves, *J. Geophys. Res.*, 102, 21,131–21,146, doi:10.1029/97JC01225.
- Plant, W. J. (2003), Microwave sea return at moderate to high incidence angles, *Waves Random Media*, 13, 339–354, doi:10.1088/0959-7174/13/4/009.
- Plant, W. J., W. C. Keller, and K. Hayes (2005), Measurement of river surface currents with coherent microwave systems, *IEEE Trans. Geosci. Remote Sens.*, 43(6), 1242–1257, doi:10.1109/TGRS.2005.845641.
- Plant, W. J., W. C. Keller, K. Hayes, and G. Chatham (2010), Normalized radar cross section of the sea for backscatter: 1. Mean levels, *J. Geophys. Res.*, 115, C09032, doi:10.1029/2009JC006078.
- Puleo, J. A., G. Farquharson, S. J. Frasier, and K. T. Holland (2003), Comparison of optical and radar measurements of surf and swash zone velocity fields, *J. Geophys. Res.*, 108(C3), 3100, doi:10.1029/2002JC001483.
- Rozenberg, A., D. Quigley, and W. Melville (1995), Laboratory study of polarized scattering by surface waves at grazing incidence: I. Wind waves, *IEEE Trans. Antennas Propag.*, 33(4), 1037–1046, doi:10.1109/36.406689.
- Rozenberg, A., D. Quigley, and W. Kendall Melville (1996), Laboratory study of polarized microwave scattering by surface waves at grazing incidence: The influence of long waves, *IEEE Trans. Geosci. Remote Sens.*, 34(6), 1331–1342, doi:10.1109/36.544557.
- Ruessink, B. G., P. S. Bell, I. M. J. van Enckevort, and S. G. J. Aarninkhof (2002), Nearshore bar crest location quantified from time-averaged X-band radar images, *Coastal Eng.*, 45, 19–32, doi:10.1016/S0378-3839(01)00042-4.
- Sletten, M. A., D. B. Trizna, and J. P. Hansen (1996), Ultrawide-band radar observations of multipath propagation over the sea surface, *IEEE Trans. Antennas Propag.*, 44(5), 646, doi:10.1109/8.496249.
- Sletten, M. A., X. Liu, J. H. Duncan, and J. C. West (2002), Radar investigations of breaking water waves at low grazing angles with simultaneous high-speed optical imagery, in *IEEE International Geoscience and Remote Sensing Symposium, 2002, IGARSS '02*, vol. 2, pp. 922–924, Springer, US, doi:10.1109/IGARSS.2002.1025730.
- Smith, J. M., E. M. Poulter, and J. McGregor (1996), Doppler radar measurements of wave groups and breaking waves, *J. Geophys. Res.*, 101, 14,269–14,282, doi:10.1029/96JC00766.
- Svendsen, I. A. (2006), *Introduction to Nearshore Hydrodynamics*, Adv. Ser. Ocean Eng., vol. 24, World Sci., River Edge, N. J.
- Thornton, E. B., and R. T. Guza (1983), Transformation of wave height distribution, *J. Geophys. Res.*, 88, 5925–5938.



- Trizna, D. B. (1991), Statistics of low grazing angle radar sea scatter for moderate and fully developed ocean waves, *IEEE Trans. Antennas Propag.*, *39*(12), 1681–1690, doi:10.1109/8.121588.
- Trizna, D. B. (1997), A model for Brewster angle damping and multipath effects on the microwave radar sea echo at low grazing angles, *IEEE Trans. Geosci. Remote Sens.*, *35*(5), 1232–1245, doi:10.1109/36.628790.
- Trizna, D. B., J. P. Hansen, P. Hwang, and J. Wu (1991), Laboratory studies of sea spikes at low grazing angles, *J. Geophys. Res.*, *96*, 12,529–12,537.
- van Dongeren, A., N. Plant, A. Cohen, D. Roelvink, M. Haller, and P. Catalán (2008), Beach Wizard: Nearshore bathymetry estimation through assimilation of model computations and remote observations, *Coastal Eng.*, *55*(12), 1016–1027, doi:10.1016/j.coastaleng.2008.04.011.
- West, J. C. (1999), Ray analysis of low-grazing scattering from a breaking water wave, *IEEE Trans. Geosci. Remote Sens.*, *37*(6), 2725–2727, doi:10.1109/36.803420.
- West, J. C., and S.-J. Ja (2002), Two-scale treatment of low-grazing-angle scattering from spilling breaker water waves, *Radio Sci.*, *37*(4), 1054, doi:10.1029/2001RS002517.
- West, J. C., J. M. Sturm, and S.-J. Ja (1998), Low-grazing scattering from breaking water waves using an impedance boundary MM/GTD approach, *IEEE Trans. Antennas Propag.*, *46*(1), 93–100, doi:10.1109/8.655455.
- Wetzel, L. (1986), On microwave scattering by breaking waves, in *Wave Dynamics and Radio Probing of the Ocean Surface*, edited by O. M. Phillips and K. Hasselmann, chap. 18, pp. 273–285, Plenum, Springer, US.
- Wetzel, L. B. (1990), Electromagnetic scattering from the sea at low grazing angles, in *Surface Waves and Fluxes*, vol. 2, edited by G. L. Garraert and W. J. Plant, chap. 12, pp. 109–172, Kluwer Acad, Springer, Netherlands.
- Wright, J. W. (1968), A new model for sea clutter, *IEEE Trans. Antennas Propag.*, *AP-16*(2), 217–223.
- Young, I. R., W. Rosenthal, and F. Ziemer (1985), A three-dimensional analysis of marine radar images for the determination of ocean wave directionality and surface currents, *J. Geophys. Res.*, *90*, 1049–1059.